Supplementary Information

Redefining Molecular Design and Exciton Dynamics in Single-Component Organic Photocatalysts for Efficient Solar-to-Hydrogen Conversion

Jae Hoon Son,[‡, a] Keren Ai,[‡, b] Jaehyeong Kim,[‡, c] Zhihao Feng,[‡, d] Rose Newman,[b] Yeonjeong Lee,[c] Stanley Cazaly,[e] Jongmin Han,[f] Myoung Hoon Song,[f] Flurin Eisner,[e] Seung Soon Jang,*[,g] Jin Young Kim,*[, c, h] James R. Durrant,*[, b] and Han Young Woo*[, a]

[a] J. H. Son, Prof. H. Y. Woo
Department of Chemistry, Korea University, Seoul 02841, Republic of Korea.
*E-mail: hywoo@korea.ac.kr

[b] K. Ai, R. Newman, Prof. J. R. Durrant
Department of Chemistry, Centre for Processable Electronics, Imperial College London, White City Campus, London, W12 0BZ, UK.
*E-mail: j.durrant@imperial.ac.uk

[c] J. Kim, Y. Lee, Prof. J. Y. Kim
School of Energy and Chemical Engineering, Ulsan National Institute of Science and Technology (UNIST), Ulsan 44919, Republic of Korea.

[d] Z. Feng
School of Chemical and Biomolecular Engineering, Georgia Institute of Technology, Atlanta, GA 30332, USA.

[e] S. Cazaly, F. Eisner
School of Engineering and Materials Science, Queen Mary University of London, London E1 4NS, UK.

[f] J. Han, Prof. M. H. Song
Department of Material Science and Engineering, Ulsan National Institute of Science and Technology (UNIST), Ulsan 44919, Republic of Korea.

[g] Prof. S. S. Jang
School of Materials Science and Engineering, Georgia Institute of Technology, Atlanta, GA 30332, USA.
*E-mail: seungsoon.jang@mse.gatech.edu

[h] Prof. J. Y. Kim
Graduate School of Carbon Neutrality, Ulsan National Institute of Science and Technology (UNIST), Ulsan 44919, Republic of Korea.
*E-mail: jykim@unist.ac.kr

[‡] These authors contributed equally to this work

General.

^1H and ^{13}C nuclear magnetic resonance (NMR) spectra were measured using a Bruker Avance III HD system operating at 500 and 125 MHz, respectively. Mass spectra were collected using a matrix-assisted laser desorption ionization time-of-flight (MALDI-TOF) (TOF™ 5800 system, AB SCIEX) in mass spectrometer (MS) reflector mode (positive) at the Korea Basic Science Institute (Seoul). The Ultraviolet-visible (UV-vis) spectra were measured with a Jasco V-630 spectrophotometer. Cyclic voltammetry (CV) data were obtained using a Versa STAT3 (Princeton Applied Research) with a three-electrode cell in 0.1 M tetrabutylammonium tetrafluoroborate (Bu_4NBF_4) in CH_3CN at a scan rate of 50 mV s^{-1} (employing a platinum wire as a counter electrode, platinum electrode coated with a thin film of active material as the working electrode, and Ag/Ag^+ electrode as a reference electrode). Mott-Schottky curves were measured by sweeping the DC potential to the working electrode with 10 mV of amplitude under dark conditions. The Mott-Schottky plots were obtained by plotting C^{-2} versus the applied potential (V) at the semiconductor/electrolyte interface. X-ray photoelectron spectroscopy (XPS) was performed using a Thermo Fisher Scientific NEXSA system with an Al Kα (1486.6 eV) microfocus monochromatic source. The Extended X-ray absorption fine structure (EXAFS) experiments were conducted at the 6D UNIST-PAL beamline in Pohang, South Korea. Attenuated total reflectance Fourier transform infrared spectroscopy (ATR FT-IR) was performed using an ALPHA II (Bruker). Contact angle (CA) measurements were carried out using a Phoenix-MT (M.A.T) system. Kelvin probe force microscopy (KPFM) measurements were performed using a MultiMode 8 system (Bruker) under ambient conditions. All measurements were conducted using conductive cantilever tips (SCM-PIT-V2, Bruker) with a resonance frequency of $f_0 = 75$ kHz and a spring constant of $k =$

$3\ N\cdot m^{-1}$. Photoelectrochemical impedance spectroscopy (PEIS) was performed on the fluorine doped tin oxide (FTO)/Pt deposited NP devices under 1 sun illumination (Xenon lamp (Newport Corporation), calibrated with a silicon photodiode). The frequency range spanned from 100 kHz to 100 Hz. The dielectric constant of the films was measured by impedance spectroscopy using parallel-plate capacitor devices (Indium tin oxide (ITO)/active layer film/Al) over a frequency range of 100 kHz to 100 Hz. 2D GIWAXS measurements were carried out at the 9A beamline (U-SAXS) at Pohang Accelerator Laboratory (beam energy: 11.06 KeV and incident angles: 0.12°), Pohang, Republic of Korea. The hydrodynamic diameters of the nanoparticles (NPs) were measured in an aqueous solution at room temperature using a dynamic light scattering (DLS) machine (BI-200SM, Brookhaven Instruments Co., USA) with a 633 nm laser. High-resolution transmission electron microscopy (HR-TEM) was performed using a Cs probe corrected JEM-2100F (JEOL, Japan) operating at 200 kV, which is equipped with a Gatan imaging filter (GIF) system. High-angle annular dark field scanning transmission electron microscopy (HAADF-STEM) was also conducted using the same instrument. Open-circuit potential (OCP) measurements were carried out with a potentiostat (IviumStat.h) in a three-electrode configuration. An Ag/AgCl (saturated KCl) electrode was used as the reference electrode, with a platinum plate serving as the counter electrode.

EXAFS analysis.

To prepare the Pt-deposited NP powder sample, excess *L*-ascorbic acid (AA) and sodium poly[2-(3-thienyl)-ethoxy-4-butylsulfonate] (TEBS) surfactant were removed using a dialysis tube (<7 kDa) for two days. After dialysis, the remaining water was removed by freeze-drying to obtain the Pt-deposited NPs. Data analysis and EXAFS fitting were performed using the Athena and Artemis programs of the Demeter data analysis packages that utilize the FEFF6 program to fit the EXAFS data. The energy calibration was conducted with Pt foil as a standard. The $\chi(\mathrm{k})$ data were extracted by subtracting a smooth, three-stage polynomial approximating the absorption background of an isolated atom. The k^2-weighted $\chi(k)$ data were Fourier transformed after applying a Hanning window function ($\Delta k = 1.0$). Nonlinear least-squares fitting of the EXAFS equation to the Fourier-transformed R-space data was conducted using Artemis to extract the coordination number (CN), interatomic distance (R), Debye–Waller factor (σ^2), and energy shift (ΔE_0). The EXAFS spectra of a Pt foil were fitted to determine the amplitude reduction factor (S_0^2), which was found to be 0.85. This S_0^2 value was then applied in the EXAFS analysis to determine the CNs for the Pt–N/Cl/Pt scattering paths in the sample.

Photocatalytic NP stock suspension preparation.

A stock solution of the photoactive small molecules was prepared by dissolving the compounds in chloroform (CF) at a concentration of 1 mg mL^{-1}. Separately, an aqueous solution of TEBS was prepared at a concentration of 10 mg mL^{-1}. To form NP suspensions, 2 mL of the CF solution, 1.6 mL of the TEBS solution, and 2.4 mL of deionized (DI) water were mixed and subjected to ultrasonication for five cycles (each consisting of 30 seconds of sonication followed by 30 seconds of rest). CF was then removed by stirring the mixture under a nitrogen flow at 80 °C for 20 minutes. After solvent removal, DI water was added to compensate for volume loss, adjusting the final volume to 4 mL. The resulting dispersion contained NPs at a concentration of 0.5 mg·mL^{-1}.

Photocatalytic H_2 evolution measurement.

An appropriate volume of the 0.5 mg·mL^{-1} NP dispersion and a corresponding volume of 0.5 mg·mL^{-1} K_2PtCl_6 solution (based on the amount of NP dispersion) were added to 21 mL gas-tight vials. The total volume was adjusted to 12 mL by adding 0.2 M AA. The vials were then sealed and purged with argon gas for 20 minutes. Photocatalytic hydrogen evolution was carried out under illumination from a 300 W Xenon arc lamp (Newport, 66984-300XF-R1) equipped with an AM 1.5G filter. The light intensity was calibrated to 1 sun (100 mW cm^{-2}) using a power meter (Newport, 1919-R) and a thermopile sensor (Newport, 919P-003-10). Evolved hydrogen gas was quantified by gas chromatography (Agilent 8890 GC) equipped with a thermal conductivity detector, using calibration standards of 1000 and 10,000 ppm hydrogen. Gas samples (1 mL) were withdrawn from the vial headspace using a gas-tight syringe (Agilent, 2.5 mL, PTFE, Luer lock). To prevent air contamination, syringe puncture points in the septa were sealed with Play-Doh clay (Hasbro, Inc.) immediately after each sampling.

Apparent quantum yield (AQY) calculation.

The AQY was calculated using the equation S1 below,

$$AQY\ (\%) = \frac{2\ \times Number\ of\ evolved\ H_2\ molecules}{Number\ of\ incident\ photons} \times\ 100$$

$$= \frac{2\ \times n\ \times\ N_A\ \times h\ \times c}{P\ \times S\ \times\ \lambda_m\ \times t} \times 100 \qquad (S1)$$

where n represents the number of moles of evolved H_2, N_A is Avogadro's number (6.022 × 10^{23}

mol^{-1}), h is Planck's constant (6.626×10^{-34} J s), and c is the speed of light (3.0×10^{8} m s^{-1}). P denotes the power of the incident light (W m^{-2}), S is the illuminated area (m^{2}), λ_{m} is the wavelength of the monochromatic light, and t is the illumination time (s). The illuminated area was 4.91 cm^{2} with a mask.

Steady-state and time-resolved photoluminescence (PL) measurements.

Steady-state PL, time-resolved PL (TRPL), and photoluminescence quantum yield (PLQY) measurements were conducted using an FLS1000 fluorescence spectrophotometer (Edinburgh Instruments), equipped with a continuous xenon lamp and both a visible-range silicon photomultiplier tube (PMT-980) and a liquid nitrogen-cooled InGaAs NIR detector (InGaAs-1650). Steady-state PL spectra were recorded under 532 nm excitation from the Xenon lamp. TRPL measurements were performed using a 635 nm diode laser (Edinburgh Instruments) operating at a repetition rate of 80 MHz. PLQY was measured under 635 nm laser excitation with the aid of an integrating sphere (diameter = 150 mm). TRPL lifetimes were obtained by deconvoluting the measured spectra with the instrument response function (IRF), followed by fitting the early-time decay ($t < 4$ ns) using a single-exponential function.

Transient absorption spectroscopy (TAS) analysis.

Femtosecond transient absorption spectroscopy (fs-TAS) measurements on NP suspensions were carried out using an amplified Ti:Sapphire laser system (Solstice, Spectra-Physics) that delivers 800 nm pulses with durations below 200 fs at a 1 kHz repetition rate. The laser output was split into pump and probe beams using a beam splitter. The pump beam was tuned to the desired excitation wavelength using an optical parametric amplifier (TOPAS Prime, Light Conversion) and a frequency mixer (NirUVis, Light Conversion). A synchronized optical chopper operating at 500 Hz modulated the pump beam. Pulse energies were monitored using an energy meter (OPHIR Photonics, VEGA P/N 7Z01560) with a 500 μm aperture. The probe beam delay was controlled via a mechanical delay stage, enabling adjustable delays of up to 6 ns relative to the pump. A white-light continuum probe, covering either the visible (450–800 nm) or near-infrared (850–1400 nm) spectral regions, was generated by focusing the probe pulse into a sapphire crystal. Before reaching the sample, the probe beam was split into two paths: one passed through the sample, and the other served as a reference. Both signals were detected using separate multichannel spectrometers equipped with Si or InGaAs detectors. Precise spatial overlap of the pump and probe beams on the sample ensured accurate measurements. All measurements were conducted under an argon atmosphere, with the NP suspensions adjusted to an absorbance of 0.5 at the excitation wavelength to ensure consistent photon absorption across samples.

Photoinduced absorption spectroscopy (PIA) measurements.

PIA measurements were conducted using a custom-built microsecond-to-second TAS system. Excitation was provided by a high-power 635 nm LED (Cree XLamp XP-E, XPERED-L1-0000-00801), powered by a precision DC power supply (TTi QL564P). The LED light was delivered to the sample via a liquid light guide. Light pulses were generated using a MOSFET transistor (STMicroelectronics STF8NM50N), with gate control managed by a data acquisition (DAQ) card (National Instruments USB-6361). Data acquisition was performed directly by the DAQ card without signal amplification. The excitation fluence was measured using a digital power meter (Thorlabs PM100) equipped with a silicon photodiode sensor (Thorlabs S120UV). All PIA kinetics were recorded under identical conditions, using 635 nm LED excitation at a fluence of 6.6 mW cm^{-2}. NP suspensions were prepared to ensure consistent photon absorption, with an absorbance of 0.6 at the excitation wavelength. All measurements were conducted under an argon atmosphere.

Exciton diffusion length calculation.

Exciton decay dynamics were analyzed using a global fitting approach based on a rate equation that accounts for both first-order exciton recombination and bimolecular exciton–exciton annihilation (EEA), as described by Equation S2,

$$\frac{dn(t)}{dt} = \kappa n(t) - \frac{1}{2}\alpha n^2(t) \quad (S2)$$

$$n(t) = \frac{n(0)e^{-\kappa t}}{1 + \frac{\alpha}{2\kappa}n(0)\left[1 - e^{-\kappa t}\right]} \quad (S3)$$

where κ represents the intrinsic fluorescence decay rate constant in the absence of exciton annihilation, while α denotes the bimolecular singlet–singlet exciton annihilation rate constant. *n(t)* corresponds to the singlet exciton density as a function of time following photoexcitation. To extract these parameters, κ was determined from TRPL measurements where exciton annihilation is negligible, corresponding to the exciton lifetime ($\tau = \kappa^{-1}$). The exciton kinetics for all NP samples were fitted using Equation S3, with α as the only free fitting parameter.

The exciton diffusion length (L_D) can be calculated using the equation S4

$$L_D = \sqrt{D\tau} \quad (S4)$$

where D is the exciton diffusion coefficient, calculated using the three-dimensional diffusion model,

$$D = \frac{\alpha}{8\pi R} \quad (S5)$$

R represents the annihilation radius of singlet excitons. A typical value of R = 1 nm was used, along with the d_{100} spacing obtained from GIWAXS measurements of the neat films, to estimate the upper and lower bounds. The results are summarized in Table S6.

Materials.

All chemicals and solvents were purchased from Aldrich, TCI, and Acros without further purification. IC2F was purchased from Solarmer.

Synthesis.

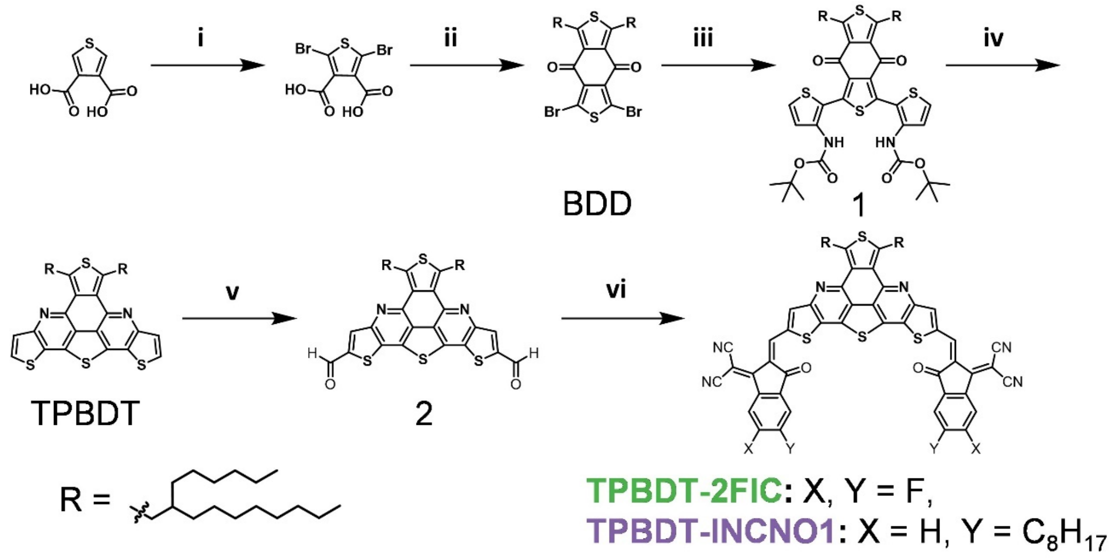

Scheme S1. Synthetic routes to two thienopyridine-fused benzodithiophene-based small molecules. i) Br$_2$, acetic acid, 72 h, ii) oxalyl chloride ((COCl)$_2$), dichloromethane (DCM), 2,5-bis(2-hexyldecyl)thiophene, AlCl$_3$, 2-dichloroethane (DCE), iii) *tert*-butyl(2-(trimethylstannyl)thiophene-3-yl)carbamate, Pd$_2$(dba)$_3$, P(*o*-tol)$_3$, tetrahydrofuran (THF): *N,N*-dimethylformamide (DMF) (10:1 *v*/*v*), 55 °C, 48 h, iv) trifluoroacetic acid, anisole, DCE, v) DMF, *n*-BuLi, THF, -78 °C, vi) 2-(5,6-difluoro-3-oxo-2,3-dihydro-1H-inden-1-ylidene)malononitrile or 5-octyl-3-dicycanovinylindan-1-one, THF, pyridine, room temperature, 3 h.

2,5-Dibromothiophene-3,4-dicarboxylic acid

Following a previously reported method,[1] bromine (11.90 mL, 232.3 mmol) was added dropwise to a mixture of thiophene-3,4-dicarboxylic acid (10 g, 58.1 mmol) and glacial acetic acid (50 mL). The reaction mixture was stirred at 50 °C for 5 days. After cooling to room temperature, a saturated $NaHSO_3$ aqueous solution was added to quench the excess bromine until the mixture became pale yellow. The resulting mixture was further cooled to 0 °C, precipitating a beige solid. The solid was filtered and washed with cold water several times, yielding a beige powder (14.2 g, 74.1%) which was used directly in the next step without further purification.

2,5-Bis(2-hexyldecyl)thiophene

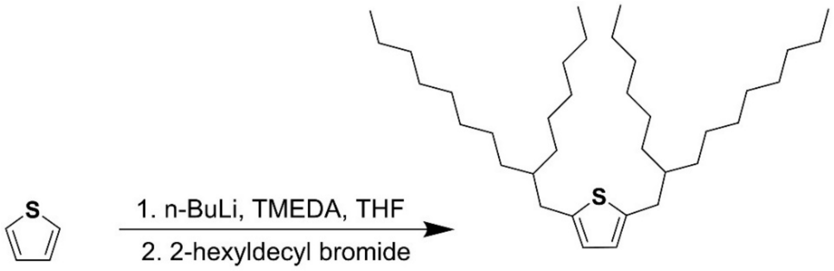

In a flame-dried 500 mL two-neck round bottom flask (RBF) under a nitrogen atmosphere, 2.0 M n-BuLi (74.3 mL, 148.55 mmol) tetrahydrofuran (THF) solution was added dropwise to thiophene (5 g, 59.42 mmol) and *N,N,N′,N′*-tetramethylethylenediamine (TMEDA) (17.27 g, 148.55 mmol) dissolved in 100 mL of anhydrous THF at -78 °C. The mixture was stirred at -78 °C for 30 minutes and then warmed to 40 °C and stirred for an additional 2 h. After cooling back to 0 °C, 2-hexyldecyl bromide (45.4 g, 148.55 mmol) was added, and the reaction mixture was stirred overnight at 40 °C. The reaction was quenched with 30 mL of water, and the product was extracted using dichloromethane (DCM). The organic phase was dried over anhydrous magnesium sulfate ($MgSO_4$), and the solvent was evaporated under reduced pressure. The product was purified via high-vacuum distillation (180 °C, 10^{-5} Torr), affording a pale yellow liquid (18.7 g, 59.0% yield). ^{1}H NMR (500 MHz, $CDCl_3$): δ (ppm) 6.52 (s, 2H), 2.67 (d, J = 6.6 Hz, 4H), 1.98 – 1.46 (m, 2H), 1.25 (m, 48H), 0.94 – 0.83 (t, 12H).

1,3-Dibromo-5,7-bis(2-hexyldecyl)-4H,8H-benzo[1,2-c:4,5-c']dithiophene-4,8-dione (BDD)

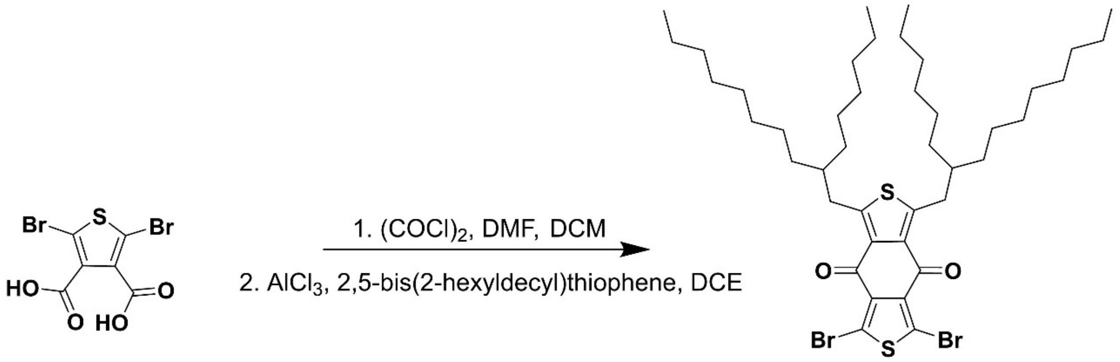

Oxalyl chloride (10.4 mL, 121.2 mmol) was added dropwise to 2,5-dibromothiophene-3,4-carboxylic acid (5.0 g, 15.2 mmol) dissolved in 30 mL of DCM and a catalytic amount of dimethylformamide (DMF, 3 drops), under a nitrogen atmosphere. The reaction mixture was stirred at room temperature for 12 h. The solvent was then removed under reduced pressure to yield crude 2,5-dibromothiophene-3,4-dicarbonyl dichloride, which was used directly in the subsequent Friedel-Crafts acylation without further purification. The crude 2,5-dibromothiophene-3,4-dicarbonyl dichloride was dissolved in 10 mL of anhydrous dichloroethane (DCE) and added dropwise to a solution of aluminum chloride ($AlCl_3$, 5.1 g, 38 mmol) in 30 mL of anhydrous DCE at −20 °C under nitrogen. After stirring the mixture for 2 h at −20 °C, 2,5-bis(2-hexyldecyl)thiophene (9.7 g, 18.2 mmol) was added slowly. The reaction was stirred at room temperature for an additional 3 h. The mixture was then quenched by slowly adding 10 mL of water at 0 °C, and the product was extracted with DCM. The organic layer was dried over anhydrous $MgSO_4$, and the solvent was evaporated under reduced pressure. The crude product was purified by silica gel column chromatography using a mixture of hexane (Hex) and DCM (1:1, *v*/*v*) as the eluent, yielding a white solid product (8.4 g, 67.7%). ^{1}H NMR (500 MHz, $CDCl_3$): δ (ppm) 3.32 (d, J = 7.2 Hz, 4H), 1.86 – 1.73 (m, 2H), 1.25 (m, 48H), 0.94 – 0.83 (t, 12H). ^{13}C NMR (125 MHz, $CDCl_3$): δ (ppm) 175.48, 155.30, 134.79, 132.76, 119.40, 39.81, 34.32, 33.54, 33.50, 31.93, 31.88, 29.99, 29.66, 29.61, 29.36, 26.47, 26.45, 22.70, 22.69, 14.14, 14.12.

Di-tert-butyl((5,7-bis(2-hexyldecyl)-4,8-dioxo-4H, 8H-benzo[1,2-c:4,5-c'] dithiophene-1,3-diyl)bis(thiophene-2,3-diyl))dicarbamate (compound 1)

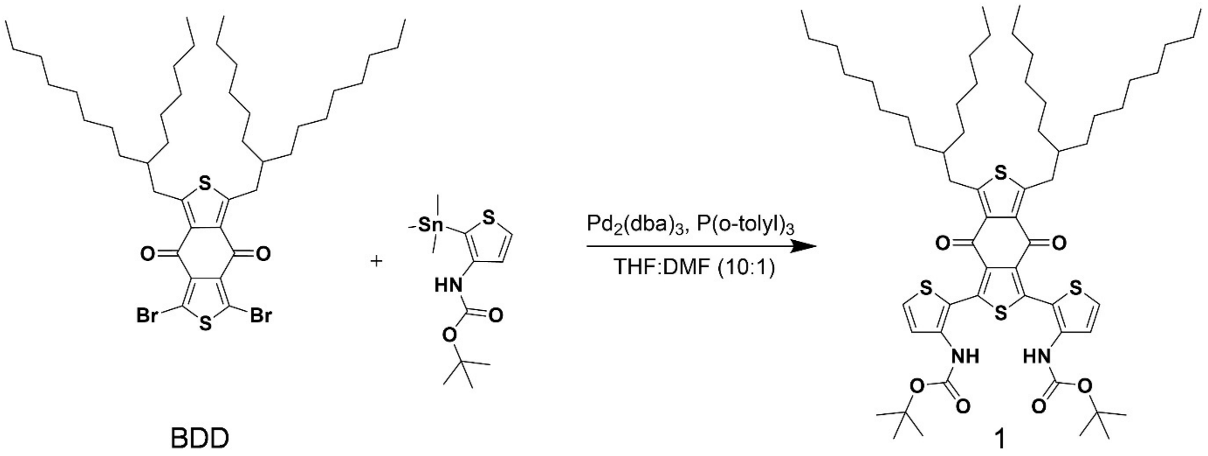

In a flame-dried one-neck round bottom flask (RBF), BDD (2.6 g, 4.88 mmol), *tert*-butyl (2-(trimethylstannyl)thiophene-3-yl)carbamate (3.89 g, 10.74 mmol), tris(dibenzylideneacetone)dipalladium(0) ($Pd_2(dba)_3$) (5 mol%), and tri(*o*-tolyl)phosphine (P(*o*-tolyl)$_3$) (10 mol%) were added. The reaction mixture was dissolved in 10 mL of anhydrous THF and 1 mL of DMF under a nitrogen atmosphere. The reaction was stirred at 50 °C for 48 h. After completion, the THF solvent was removed under reduced pressure. The residue was extracted with DCM, and the organic layer was dried over anhydrous $MgSO_4$. Following solvent removal under reduced pressure, the crude product was purified via column chromatography using a mixture of Hex and DCM (3:7, *v*/*v*) as the eluent, yielding a red sticky liquid product (2.5 g, 74.8% yield). ^{1}H NMR (500 MHz, $CDCl_3$): δ (ppm) 7.62 (br, 2H), 7.41 (d, 2H), 3.34 – 3.22 (m, 4H), 1.82 (m, 2H), 1.49 (s, 18H), 1.48 – 1.17 (m, 48H), 0.87 (t, 12H).

^{13}C NMR (125 MHz, CDCl$_3$): δ (ppm) 179.06, 154.94, 153.20, 142.41, 137.63, 134.36, 133.05, 127.20, 125.09, 116.37, 80.56, 39.70, 34.35, 33.79, 31.94, 31.92, 30.03, 29.69, 29.65, 29.33, 28.32, 26.61, 26.58, 22.69, 22.66, 14.13.

5,7-Bis(2-hexyldecyl)tetrathieno[2,3-b:3',4'-f:3'',2''-j:2''',3''',4''',5'''-lmn][4,7]phenanthroline (TPBDT)

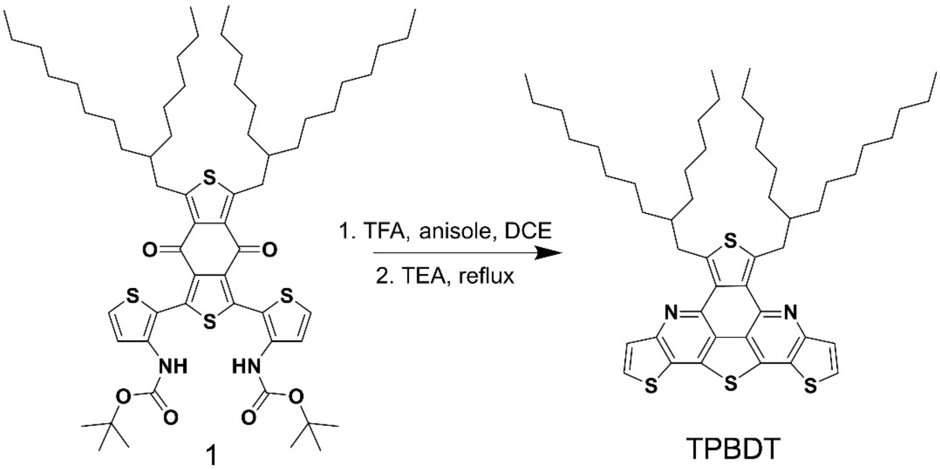

Trifluoroacetic acid (TFA) (12.5 mL) was added to a solution of compound 1 (2.5 g, 2.35 mmol) and anisole (1 mL) in 10 mL of dry DCE under an inert N$_2$ atmosphere. The reaction mixture was refluxed for 12 h with constant stirring. Upon completion, the organic solvent was removed under reduced pressure. The residue was thoroughly dried, followed by the slow addition of triethylamine (TEA) (3 mL), and the mixture was refluxed for an additional 3 h. After cooling to room temperature, the reaction mixture was poured into cold methanol (MeOH), precipitating a brown solid. The solid was collected by filtration, washed with MeOH, and further purified by silica gel column chromatography using a Hex: DCM (9:1, v/v) mixed solvent as an eluent, yielding a pale yellow solid (1.2 g, 61.7% yield). ^{1}H NMR (500 MHz, CDCl$_3$): δ (ppm) 7.82 (d, J = 5.4 Hz, 2H), 7.81 (d, J = 5.4 Hz, 2H), 3.83 (d, 4H), 2.12 (m, 2H), 1.48 – 1.16 (m, 48H), 0.92 – 0.75 (m, 12H). ^{13}C NMR (125 MHz, CDCl$_3$): δ (ppm) 155.07, 145.65, 141.98, 138.66, 132.01, 127.94, 126.51, 123.98, 123.69, 39.53, 34.52, 33.79, 33.73, 32.14, 32.09, 30.40, 30.09, 29.86, 29.55, 26.72, 22.87, 22.84, 14.27.

5,7-Bis(2-hexyldecyl)tetrathieno[2,3-b:3',4'-f:3'',2''-j:2''',3''',4''',5'''-lmn][4,7]phenanthroline-2,10-dicarbaldehyde (compound 2)

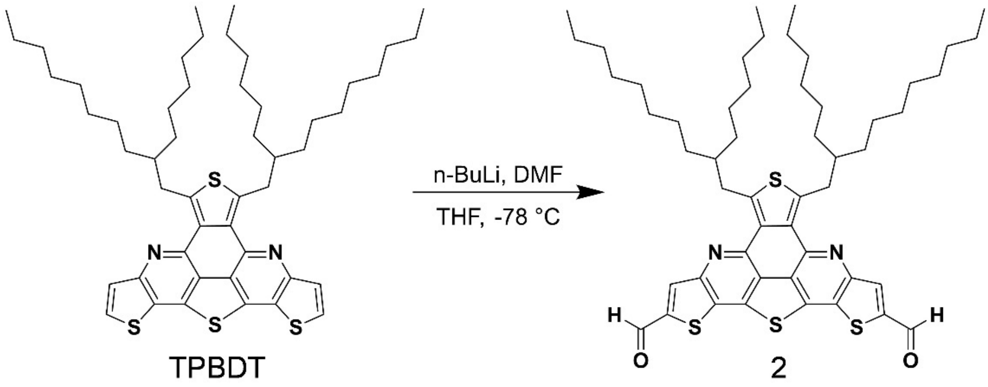

To a flame-dried two-neck RBF containing TPBDT (0.80 g, 0.97 mmol) in 6 mL of anhydrous THF under a nitrogen atmosphere, a 2.0 M solution of n-BuLi (2.0 mL, 4.06 mmol) in THF was added dropwise at -10 °C. The reaction mixture was stirred for 1.5 h at -10 °C, followed by an additional 2 h at RT. The temperature was then lowered to -78 °C, and DMF (0.75 mL, 9.7 mmol) was added dropwise. After stirring the mixture for 12 h at RT, the reaction was quenched and extracted using a DCM and water mixture. The organic phase was dried over anhydrous $MgSO_4$ and concentrated under reduced pressure. The crude product was purified by column chromatography using a CF and DCM (7:3, *v*/*v*) mixed solvent as the eluent, affording a yellow solid (0.51 g, 59.7% yield). ^{1}H NMR (500 MHz, $CDCl_3$): δ (ppm) 10.24 (s, 2H), 8.34 (s, 2H), 3.66 (d, 4H), 2.01 (m, 2H), 1.49 – 1.19 (m, 48H), 0.97 – 0.76 (m, 12H). ^{13}C NMR (125 MHz, $CDCl_3$): δ (ppm) 183.98, 153.52, 147.06, 144.15, 143.97, 139.43, 135.52, 131.03, 128.15, 125.43, 39.37, 34.47, 33.68, 33.59, 32.06, 31.96, 30.24, 29.93, 29.79, 29.42, 26.65, 22.74, 22.70, 14.16, 14.13. MS (MALDI-TOF) m/z: $[M+H]^+$ Calcd for $C_{52}H_{71}N_2O_2S_4^+$, 883.4393; found 883.3878.

TPBDT-2FIC

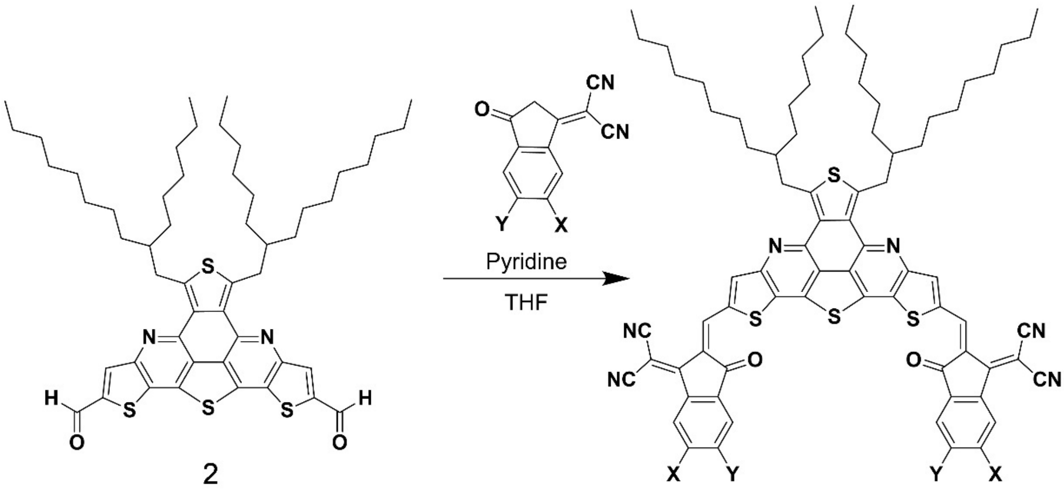

2

TPBDT- 2FIC / X, Y = F
TPBDT- INCNO1 / X = H, Y = C_8H_{17}

In a flame-dried 50 mL one-neck RBF, compound 2 (80.0 mg, 0.091 mmol), 2-(5,6-difluoro-3-oxo-2,3-dihydro-1H-inden-1-ylidene)malononitrile (IC2F, 52.1 mg, 0.226 mmol), and 10 mL of anhydrous THF were added under a nitrogen atmosphere. Subsequently, 0.2 mL of anhydrous pyridine was added dropwise at RT via syringe. The reaction mixture was stirred for two h at RT and then extracted with water and CF mixture. The organic layer was collected, dried over anhydrous $MgSO_4$, and the solvent was removed by rotary evaporation under reduced pressure. The crude product was purified by silica column chromatography using a CF:Hex (9:1, *v*/*v*) mixed solvent as the eluent. Further purification was performed via recrystallization using chloroform and methanol, yielding a black solid (52 mg, 43.9%). ^{1}H NMR (500 MHz, $CDCl_3$): δ (ppm) 8.79 (s, 2H), 8.46 (dd, 2H), 8.11 (s, 2H), 7.57 (dd, 2H), 3.76

(br, 4H), 2.02 (br, 2H), 1.49 – 1.19 (m, 48H), 0.82 (m, 12H). MS (MALDI-TOF) m/z: $[M+H]^+$ Calcd for $C_{76}H_{75}F_4N_6O_2S_4^+$, 1307.4765; found 1307.4126

TPBDT-INCNO1

The synthesis procedure for TPBDT-INCNO1 followed a similar protocol to that of TPBDT-2FIC, using 5-octyl-3-dicyanovinylindan-1-one (INCNO1) (138.7 mg, 0.226 mmol) as the terminal moiety, yielding 82.1 mg of product (62.0% yield). ^{1}H NMR (500 MHz, $CDCl_3$): δ (ppm) 8.83 (d, J = 0.8 Hz, 2H), 8.49 (d, J = 8.1 Hz, 2H), 8.11 (d, J = 0.8 Hz, 2H), 7.67 (d, J = 1.6 Hz, 2H), 7.55 (dd, J = 8.1, 1.6 Hz, 2H), 3.66 (br, 4H), 2.72 (t, 4H), 1.95 (br, 2H), 1.68 (m, 4H), 1.46 – 1.13 (m, 68H), 0.91 (t, 6H), 0.82 (m, 12H). ^{13}C NMR (125 MHz, $CDCl_3$): δ (ppm) 187.75, 158.33, 158.30, 152.46, 151.99, 147.30, 145.13, 141.68, 138.66, 137.90, 137.79, 136.99, 136.23, 132.31, 130.82, 126.53, 125.42, 123.53, 114.00, 113.73, 113.71, 71.32, 39.74, 36.29, 34.56, 33.85, 33.71, 31.95, 31.92, 31.88, 30.65, 30.20, 29.89, 29.71, 29.43, 29.37, 29.26, 26.83, 26.81, 22.75, 22.70, 22.69, 14.12, 14.11. MS (MALDI-TOF) m/z: $[M+H]^+$ Calcd for $C_{92}H_{111}N_6O_2S_4^+$, 1459.7646; found 1459.6758.

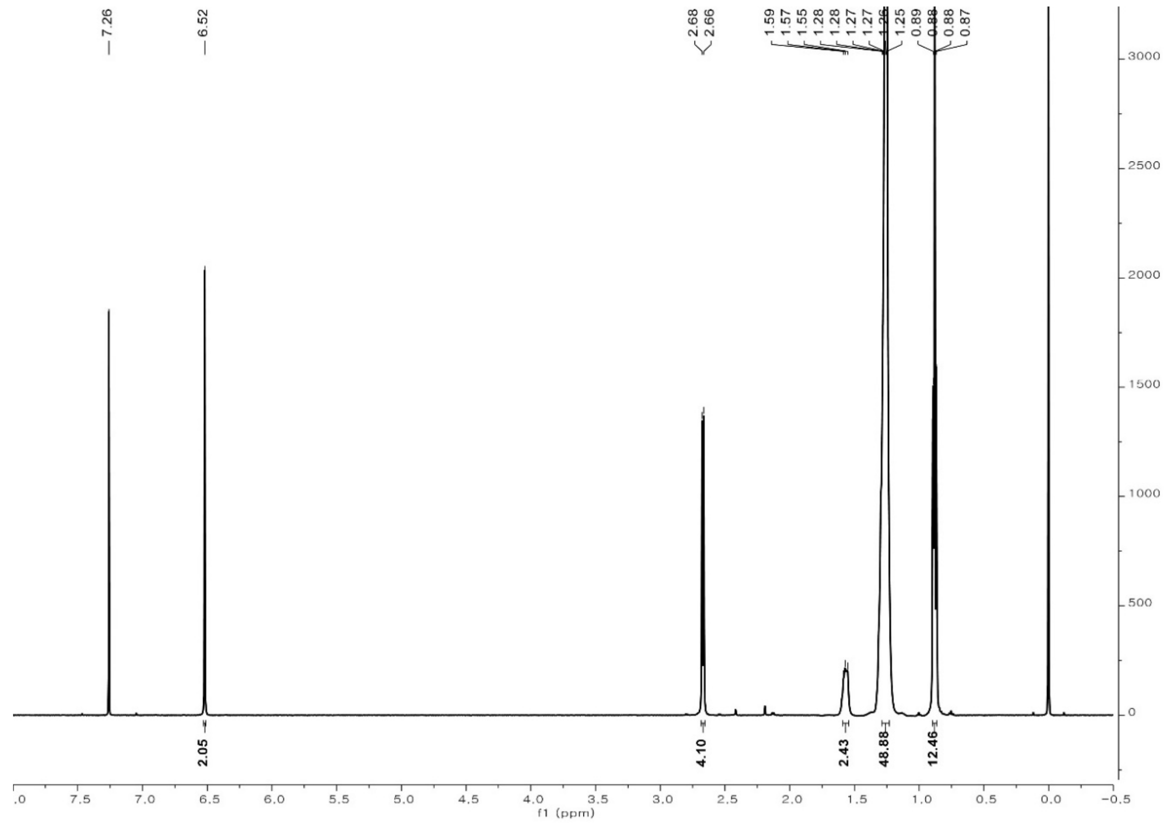

Fig. S1 ^{1}H NMR spectrum of 2,5-bis(2-hexyldecyl)thiophene in $CDCl_3$.

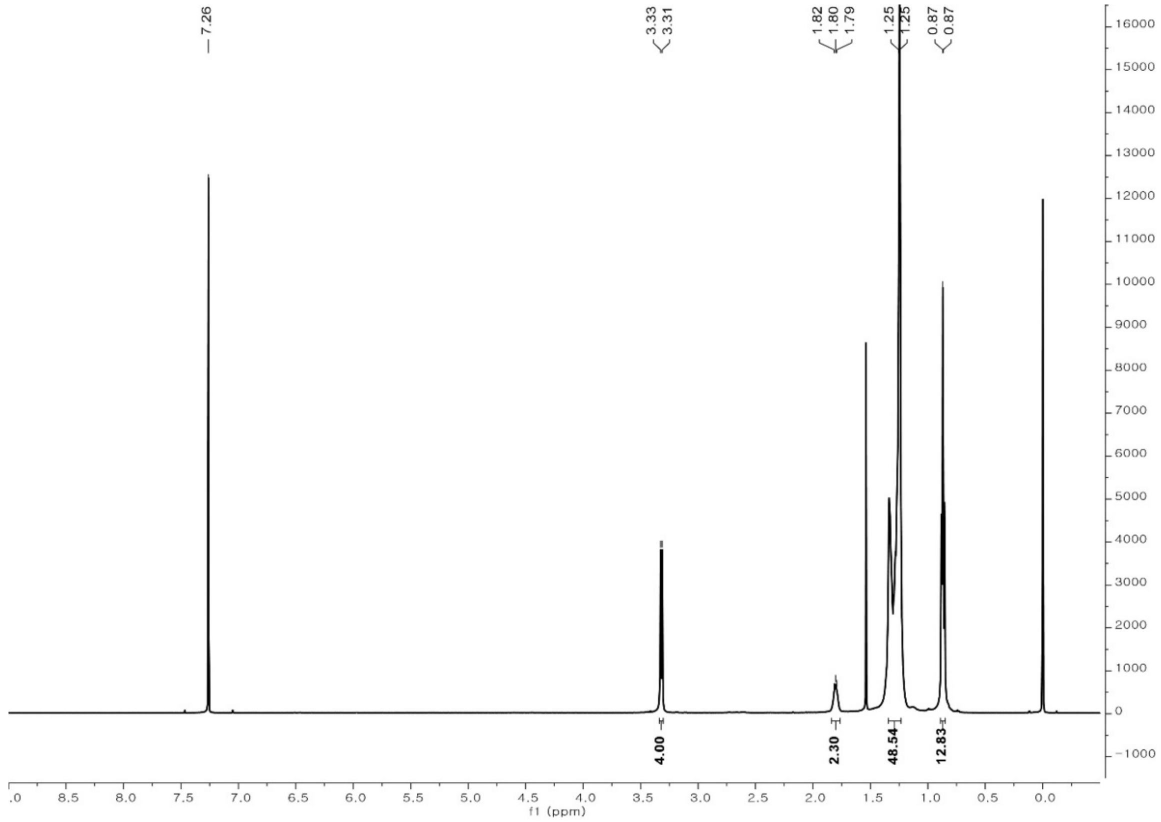

Fig. S2 ^{1}H NMR spectrum of BDD in $CDCl_3$.

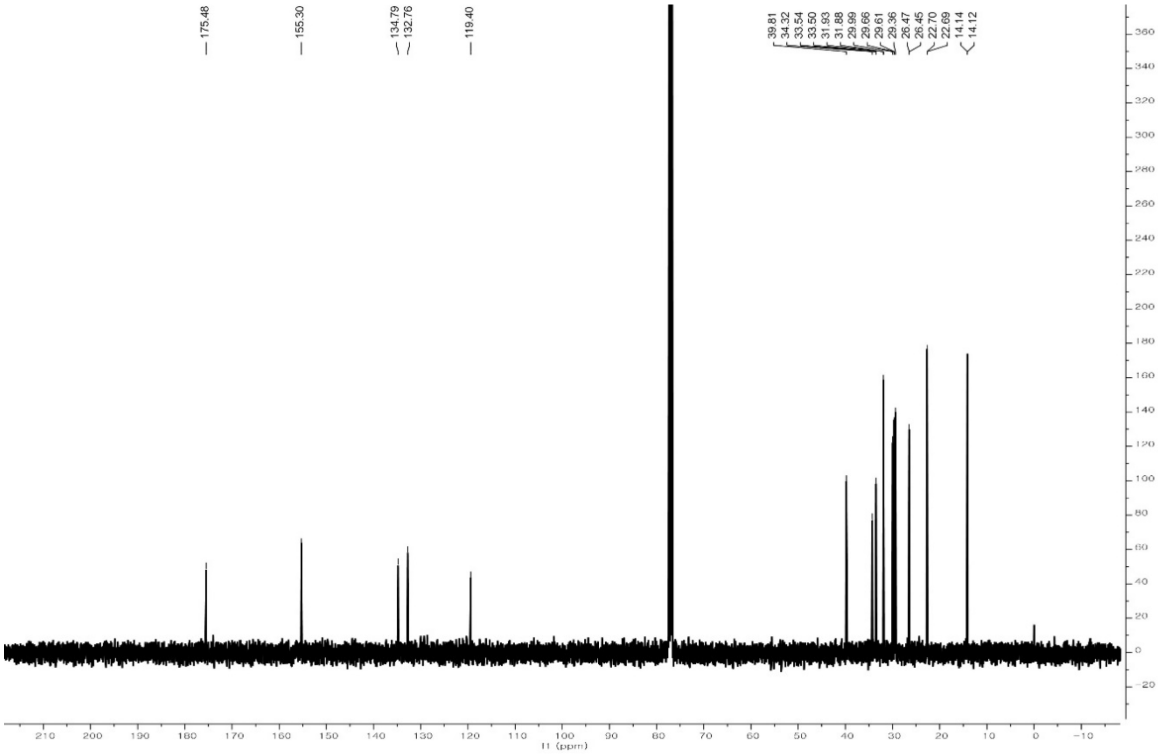

Fig. S3 ^{13}C NMR spectrum of BDD in CDCl$_3$.

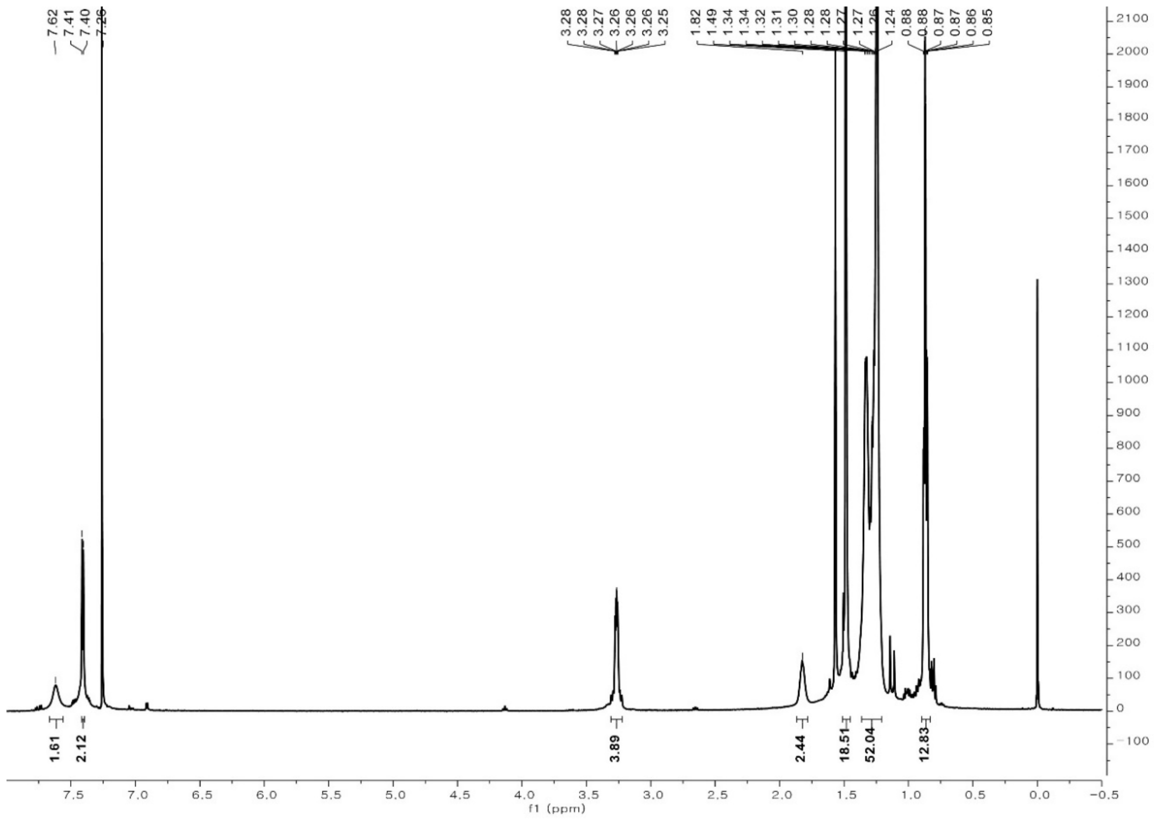

Fig. S4 ^{1}H NMR spectrum of compound 1 in $CDCl_3$.

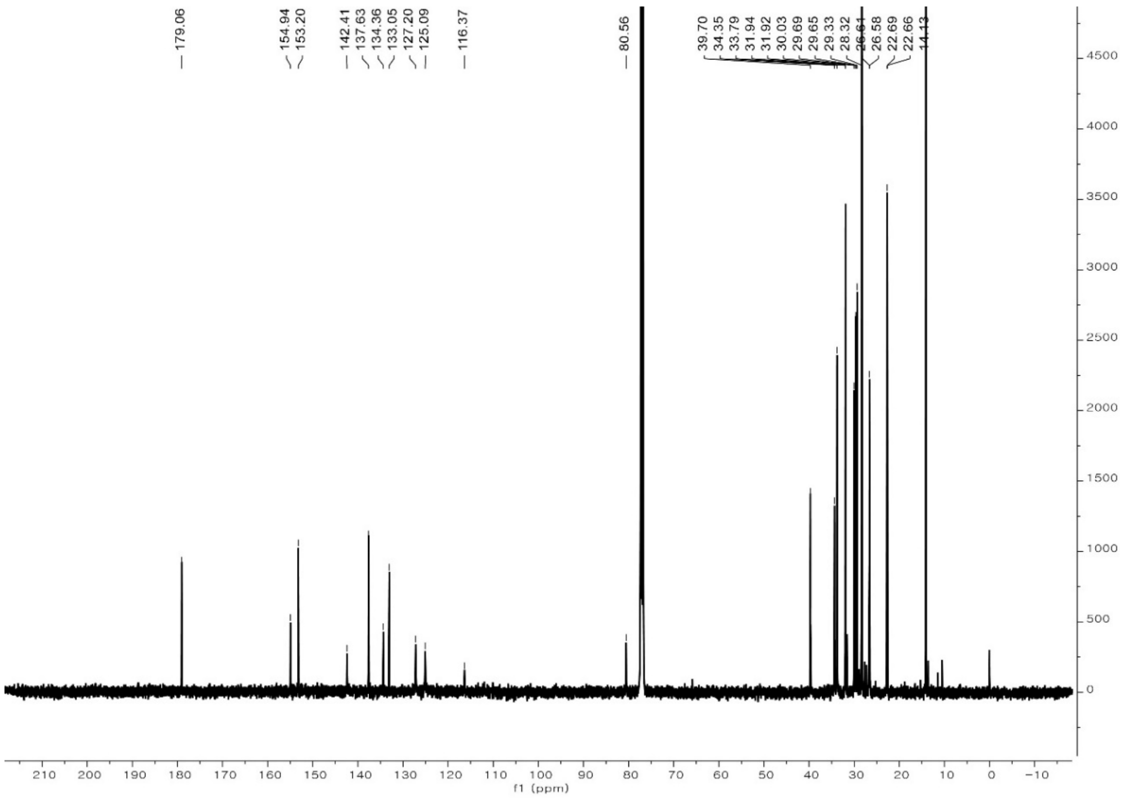

Fig. S5 ^{13}C NMR spectrum of compound 1 in $CDCl_3$.

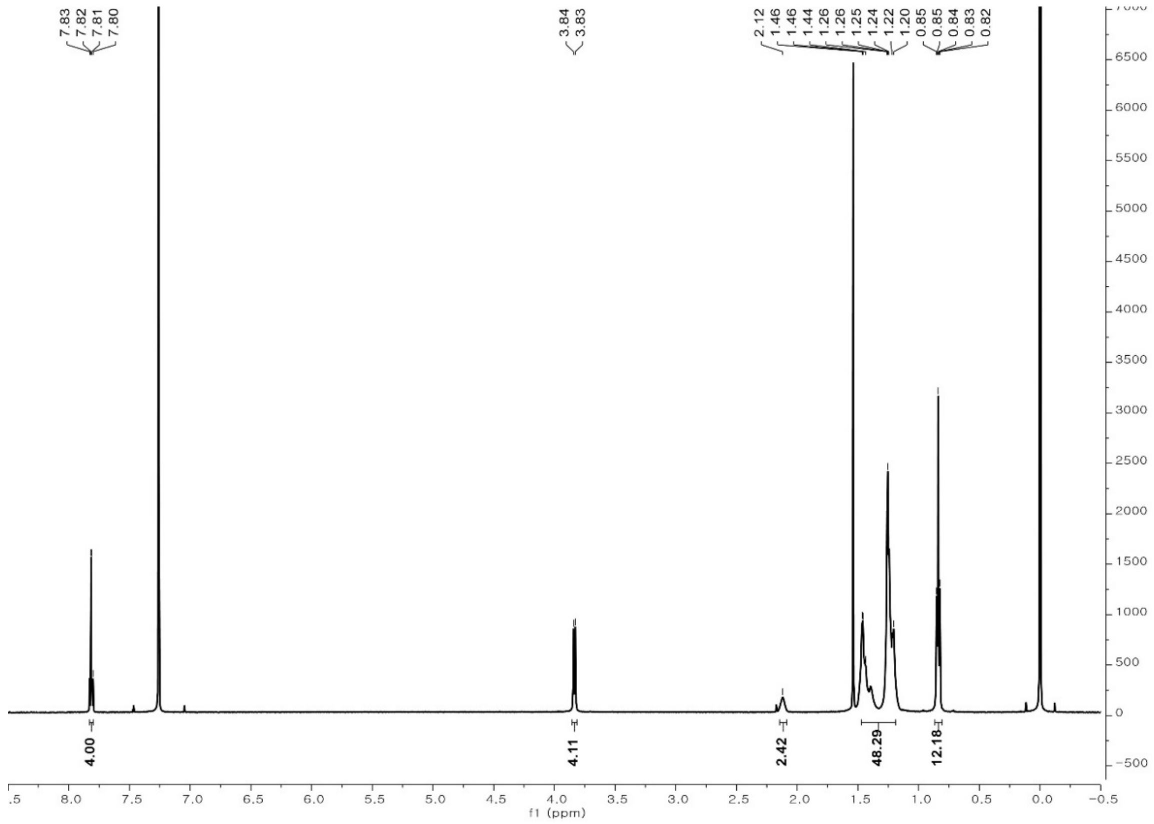

Fig. S6 ^{1}H NMR spectrum of TPBDT in $CDCl_3$.

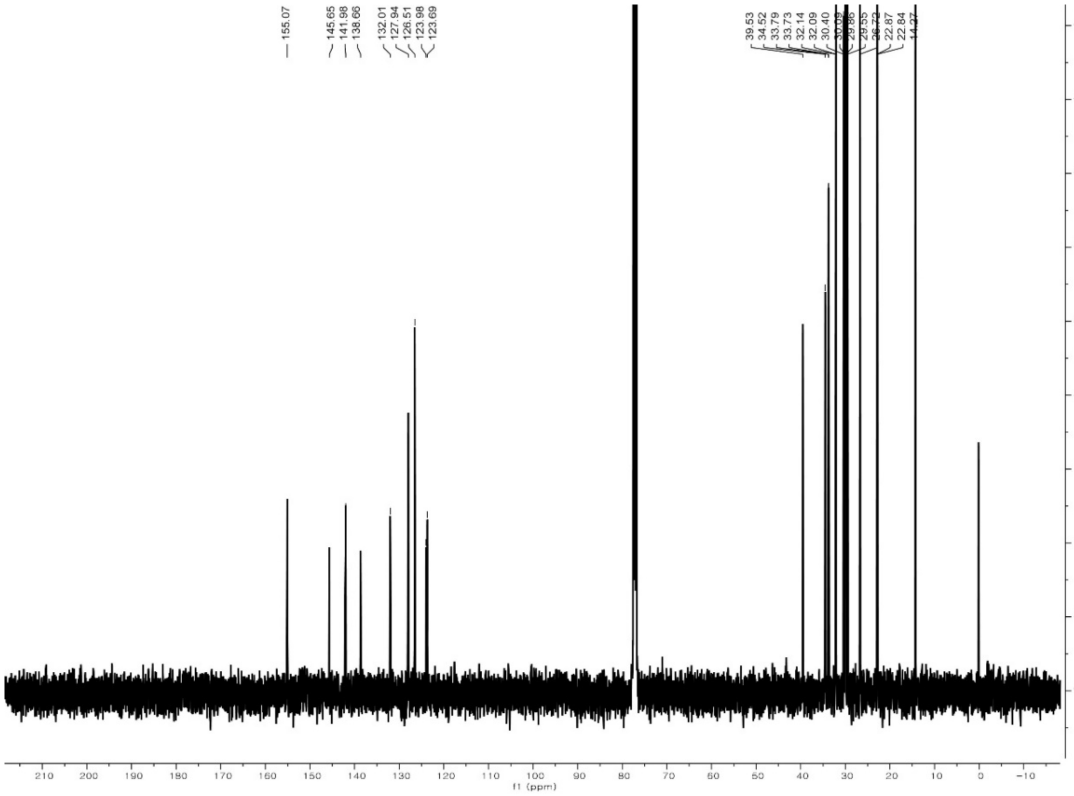

Fig. S7 ^{13}C NMR spectrum of TPBDT in $CDCl_3$.

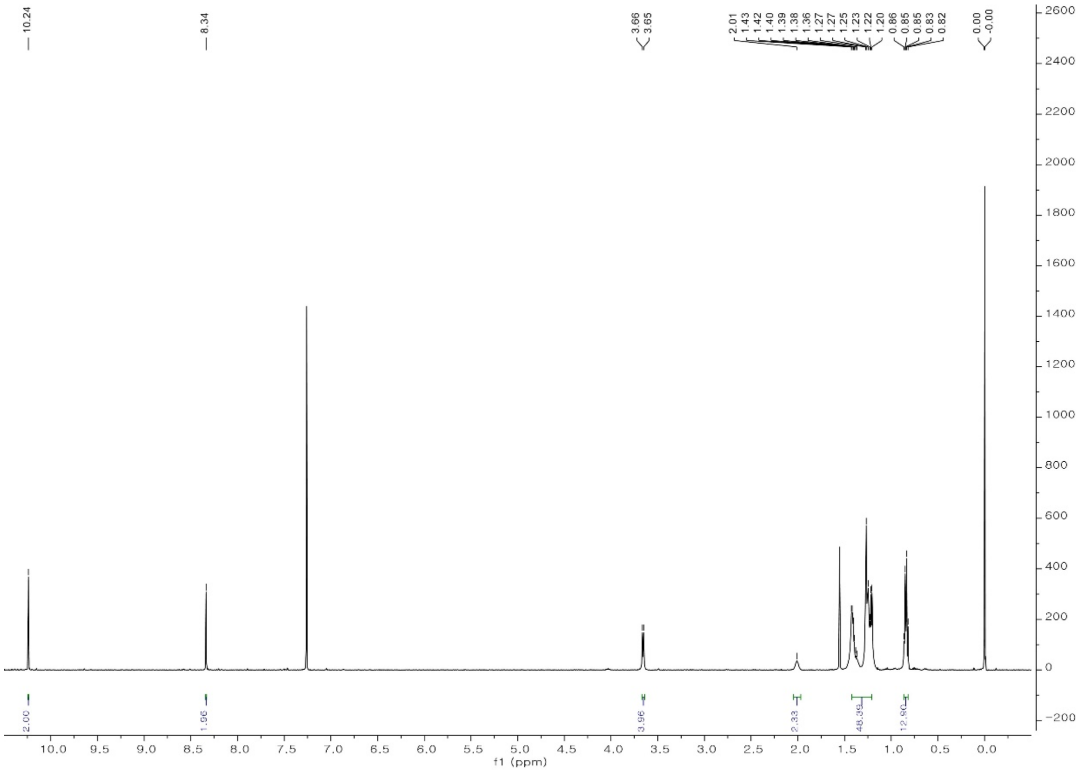

Fig. S8 ^{1}H NMR spectrum of compound 2 in $CDCl_3$.

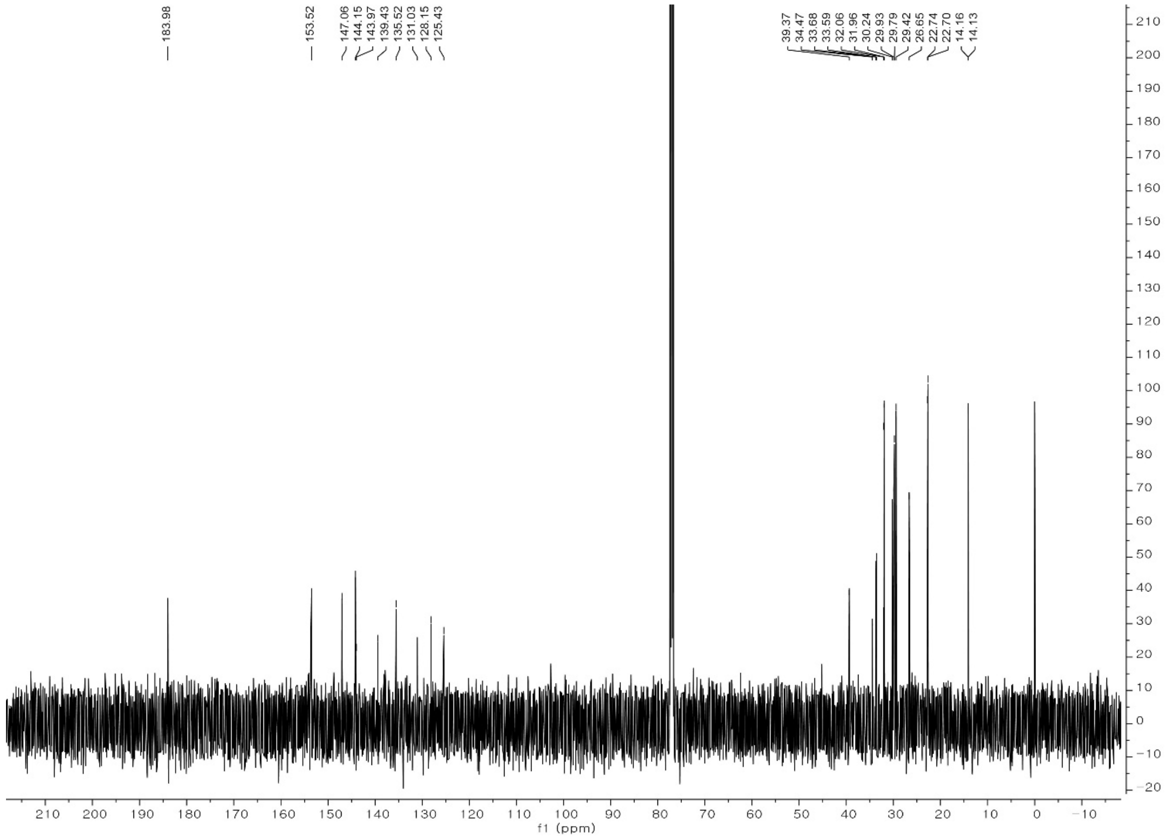

Fig. S9 ^{13}C NMR spectrum of compound 2 in $CDCl_3$.

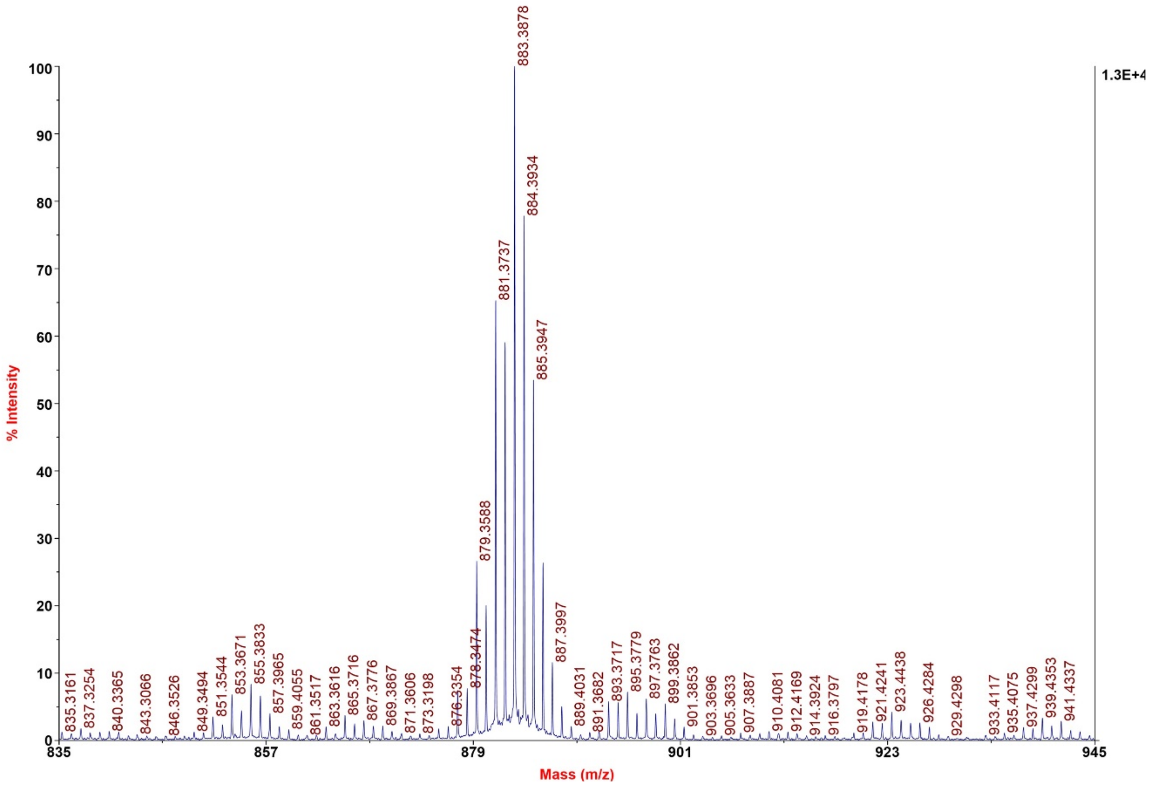

Fig. S10 MALDI-TOF spectrum of compound 2.

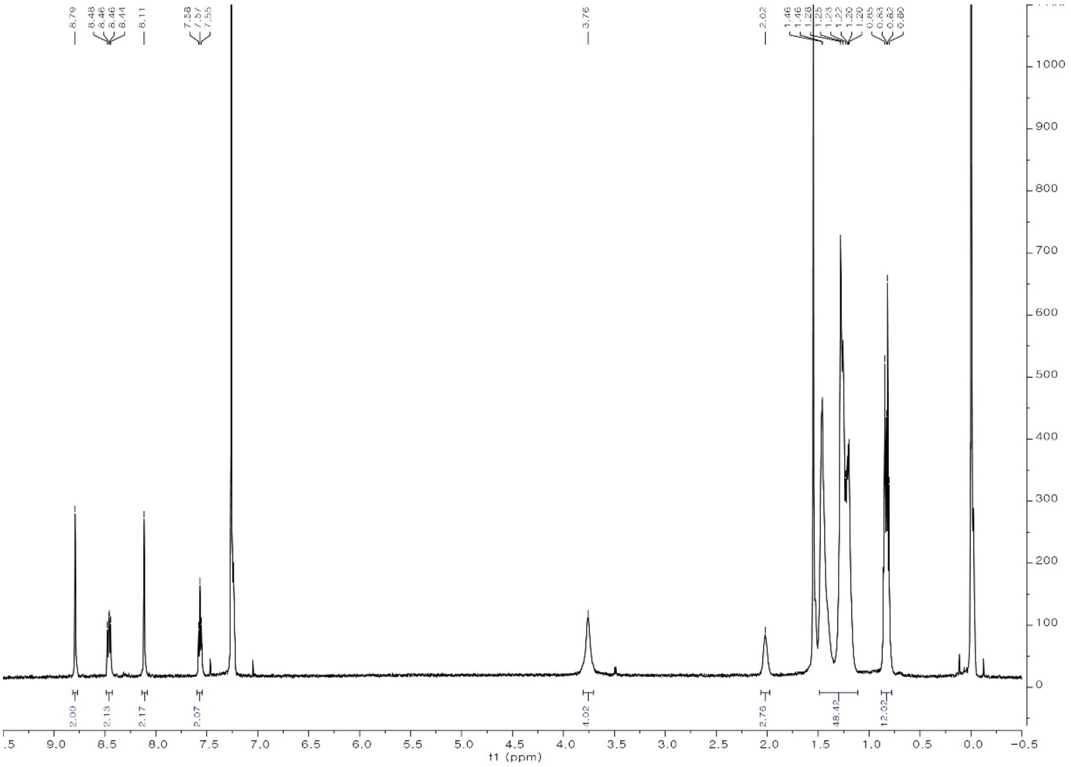

Fig. S11 ^{1}H NMR spectrum of TPBDT-2FIC in $CDCl_3$.

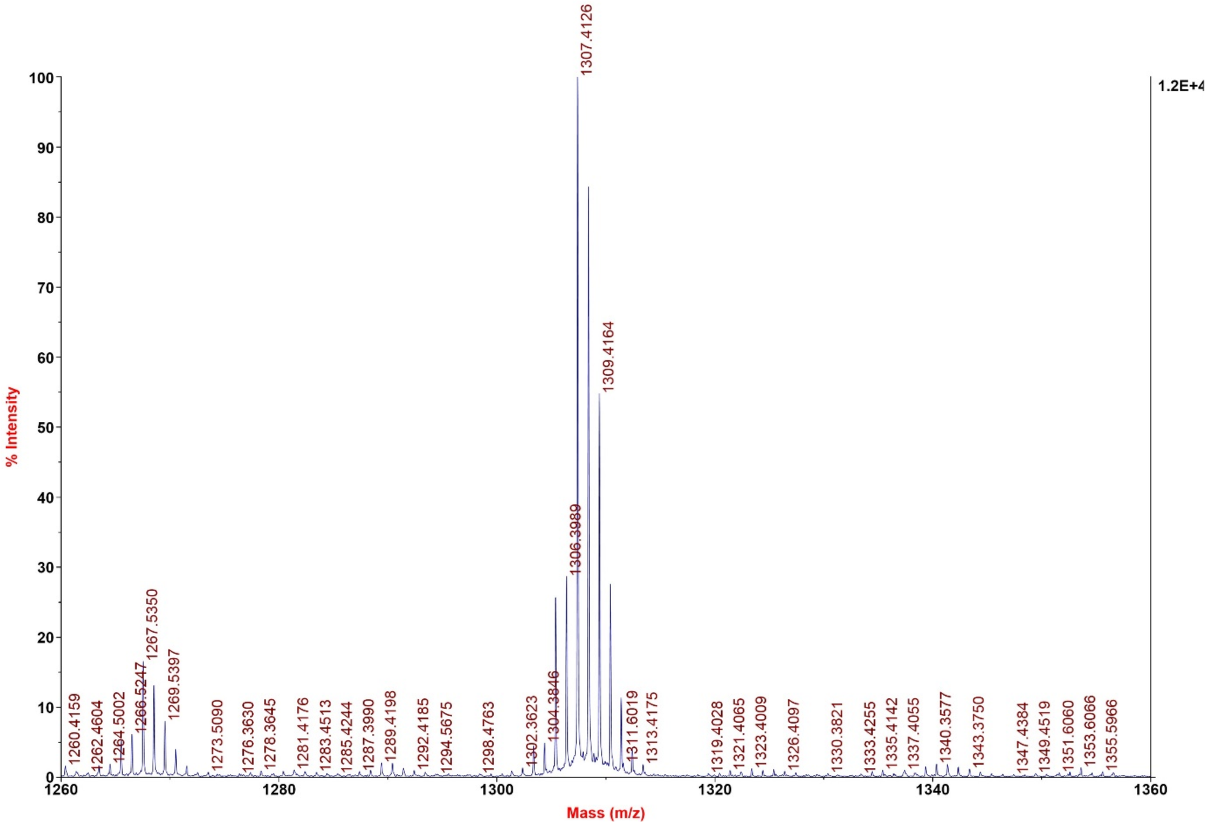

Fig. S12 MALDI-TOF spectrum of TPBDT-2FIC.

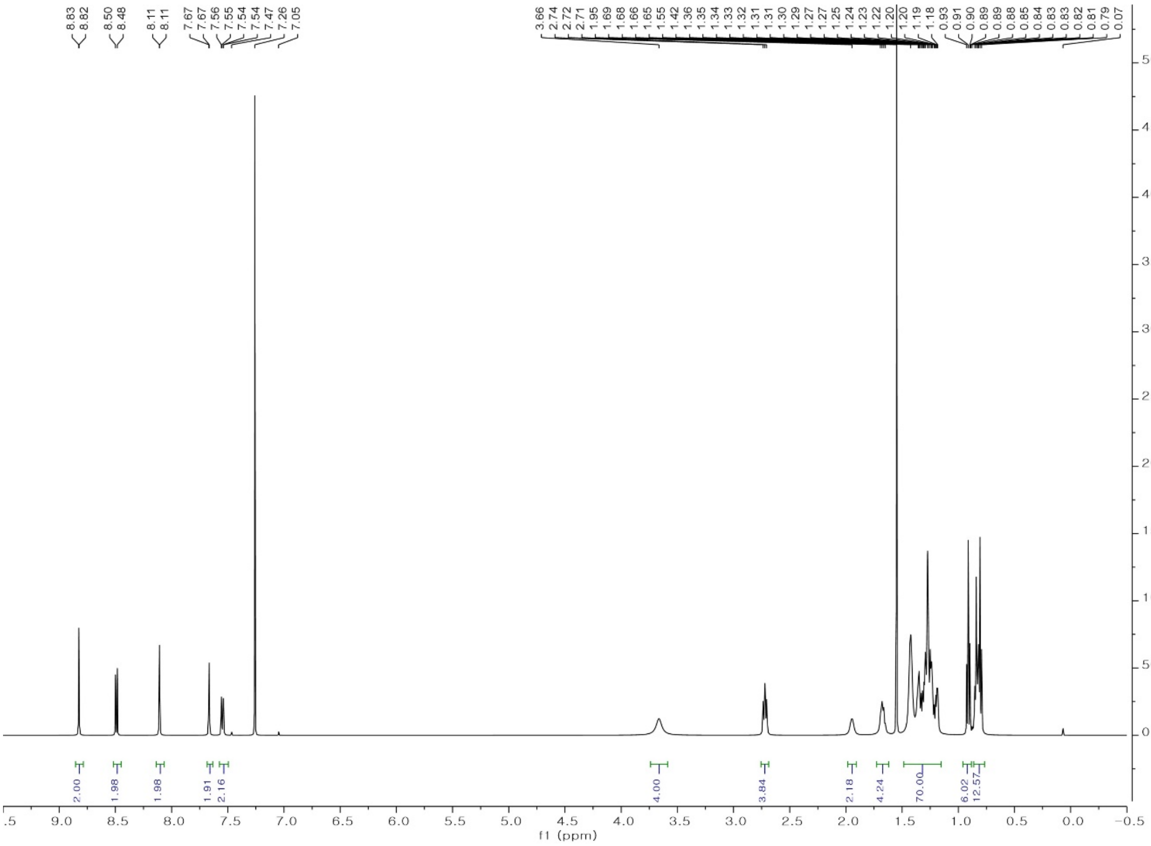

Fig. S13 ^{1}H NMR spectrum of TPBDT-INCNO1 in $CDCl_3$.

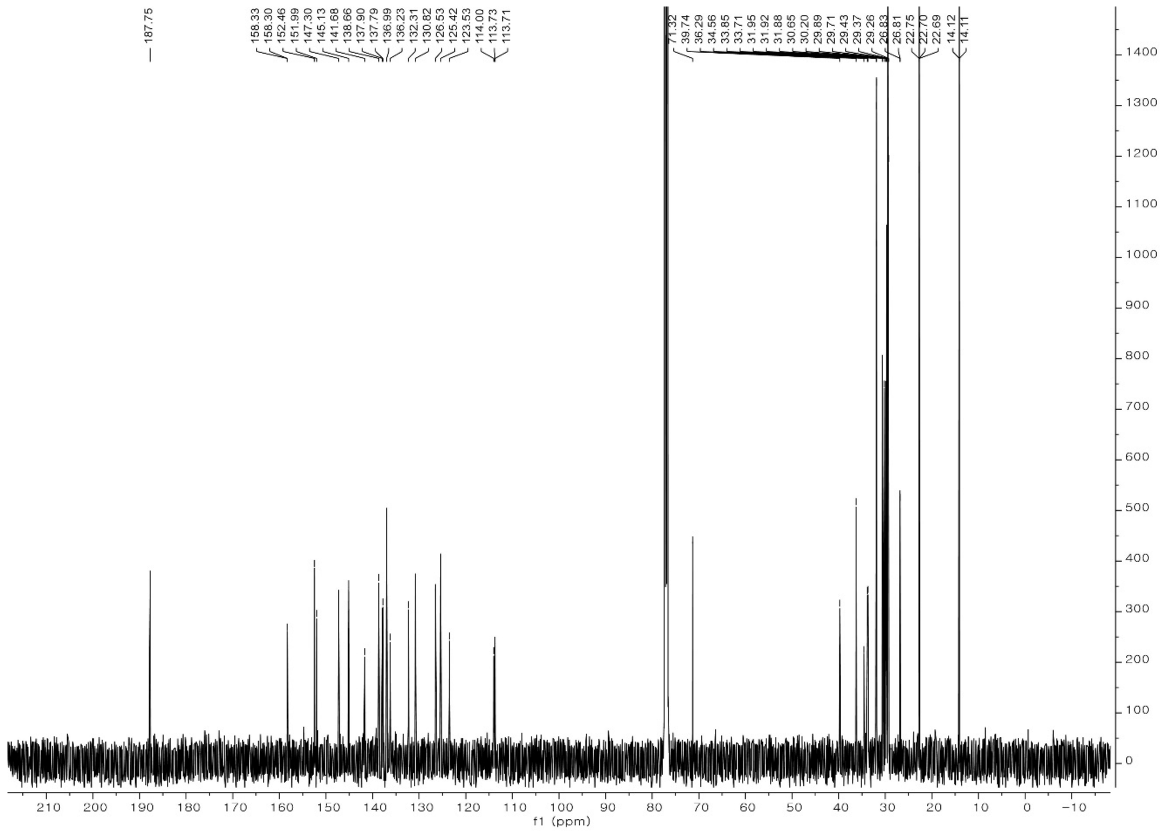

Fig. S14 ^{13}C NMR spectrum of TPBDT-INCNO1 in $CDCl_3$.

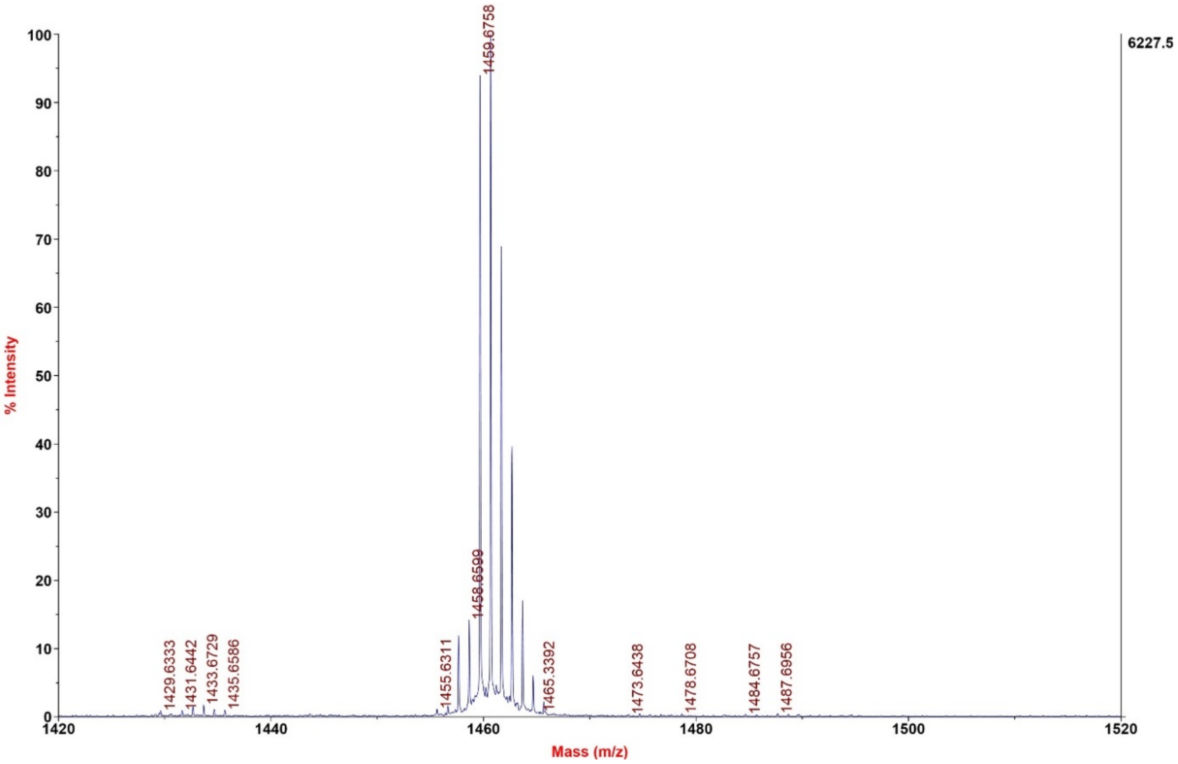

Fig. S15 MALDI-TOF spectrum of TPBDT-INCNO1.

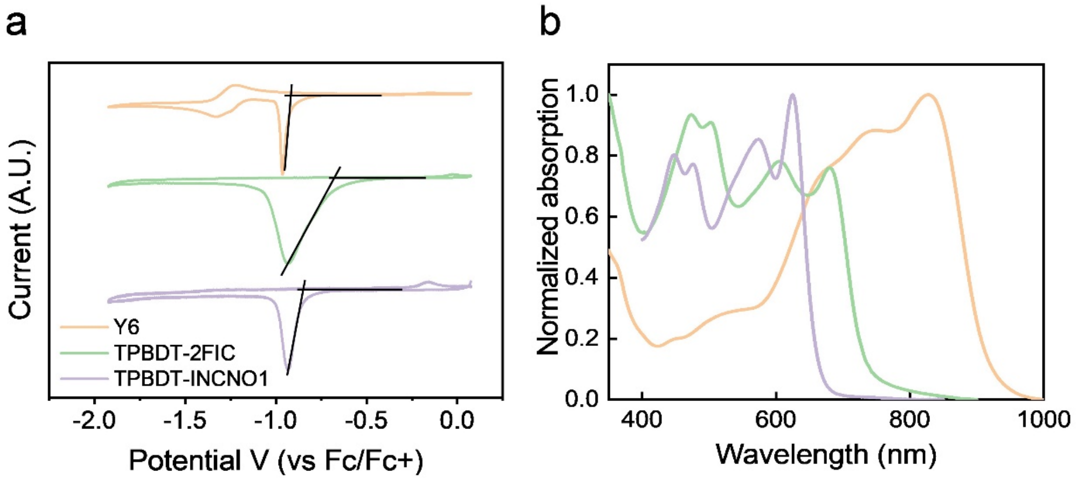

Fig. S16 (a) Cyclic voltammograms of Y6, TPBDT-2FIC, and TPBDT-INCNO1 films on a platinum working electrode in 0.1 M Bu_4NBF_4/CH_3CN, and (b) normalized UV−vis absorption spectra of Y6, TPBDT-2FIC, and TPBDT-INCNO1 thin films. The LUMO energy levels (E_{LUMO}) were estimated using the relation: $E_{\mathrm{LUMO}} = -\left(E_{\mathrm{red}} - \frac{(E_{Fc}^{Ox} + E_{Fc}^{Red})}{2} + 4.8\right)$.[2]

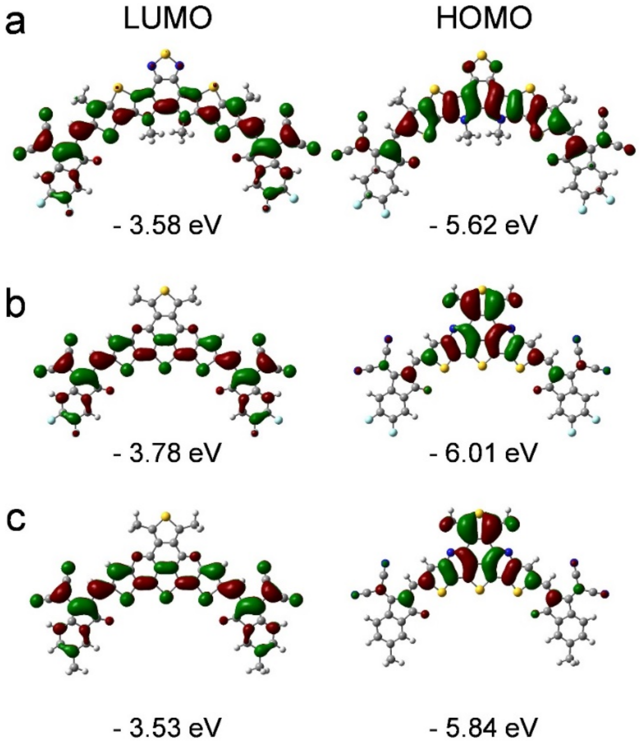

Fig. S17 Frontier molecular orbitals of (a) Y6, (b) TPBDT-2FIC, and (c) TPBDT-INCNO1 by DFT (B3LYP/6-31G basis set). Alkyl chains were replaced with methyl substituents to reduce computational costs.

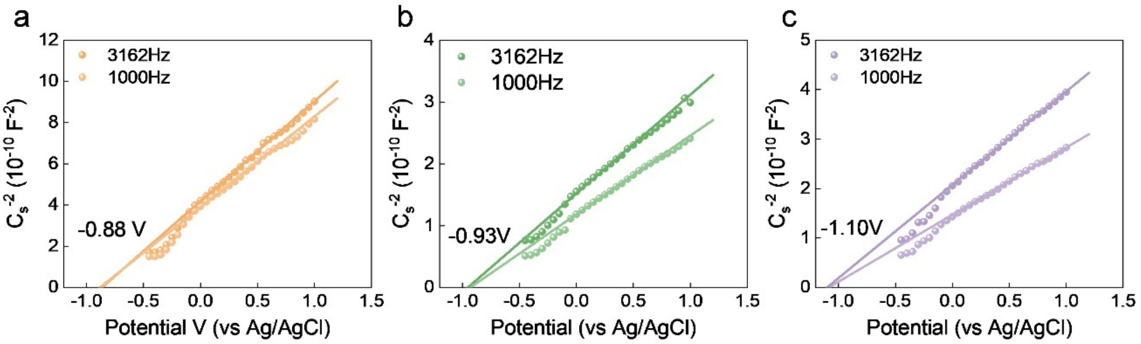

Fig. S18. Mott-Schottky plots (C^{-2}-V) of (a) Y6, (b) TPBDT-2FIC, and (c) TPBDT-INCNO1 NPs measured in an aqueous electrolyte at pH 7 using an Ag/AgCl reference electrode.

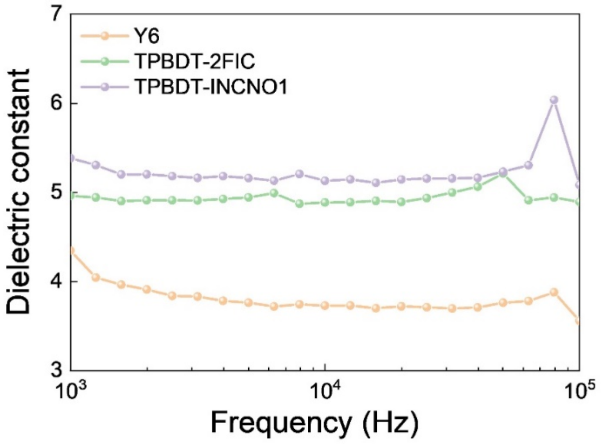

Fig. S19 Dielectric constant measurement of Y6, TPBDT-2FIC and TPBDT-INCNO1.

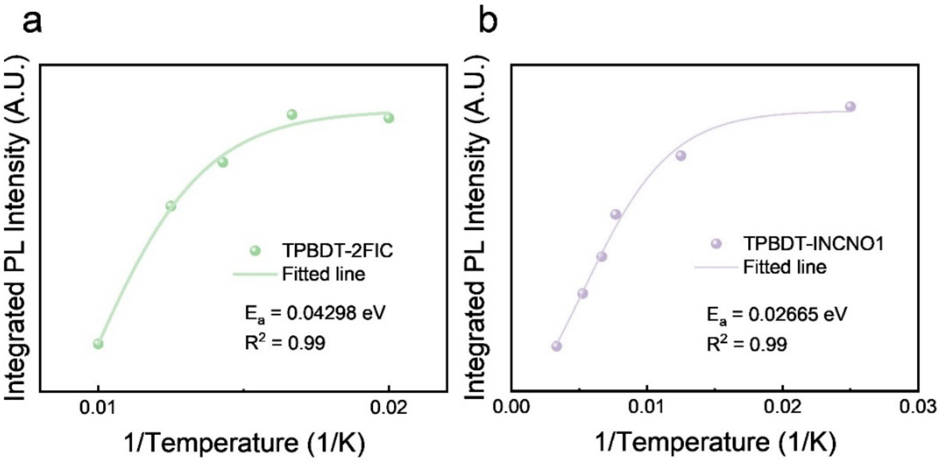

Fig. S20 Temperature-dependent PL intensity of (a) TPBDT-2FIC and (b) TPBDT-INCNO1 films measured over the temperature range of 77–250 K. The extracted exciton binding energies (E_a) are indicated in the figure.

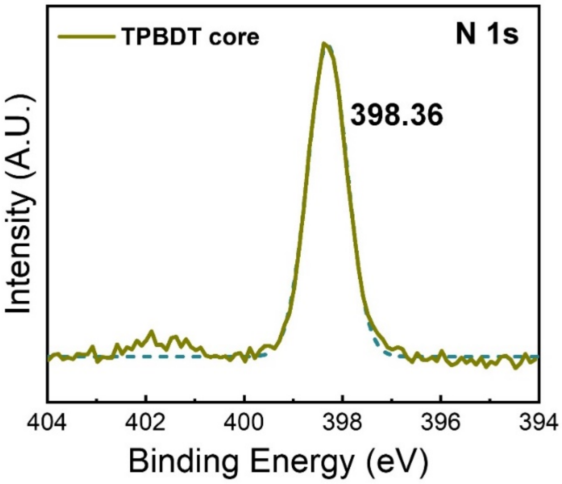

Fig. S21 XPS N 1s spectrum of TPBDT core in film.

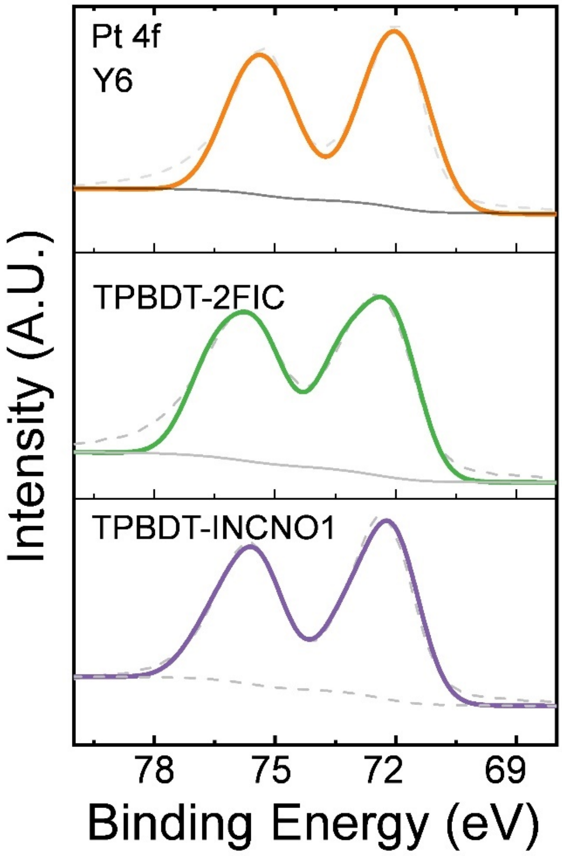

Fig. S22 XPS Pt 4f spectra of Y6 and TPBDT-2FIC and TPBDT-INCNO1 films after Pt deposition under 0.2 M AA and 1 sun light illumination.

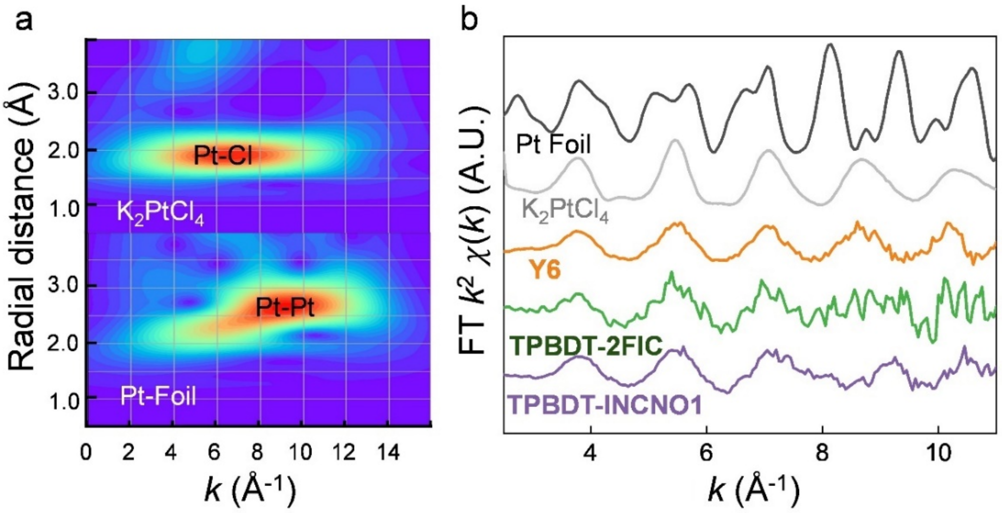

Fig. S23 (a) WT-EXAFS of Pt-foil and K_2PtCl_4 and (b) k^2-weighted FT-EXAFS spectra of reference Pt (Pt foil and K_2PtCl_4), Y6, TPBDT-2FIC and TPBDT-INCNO1 NPs.

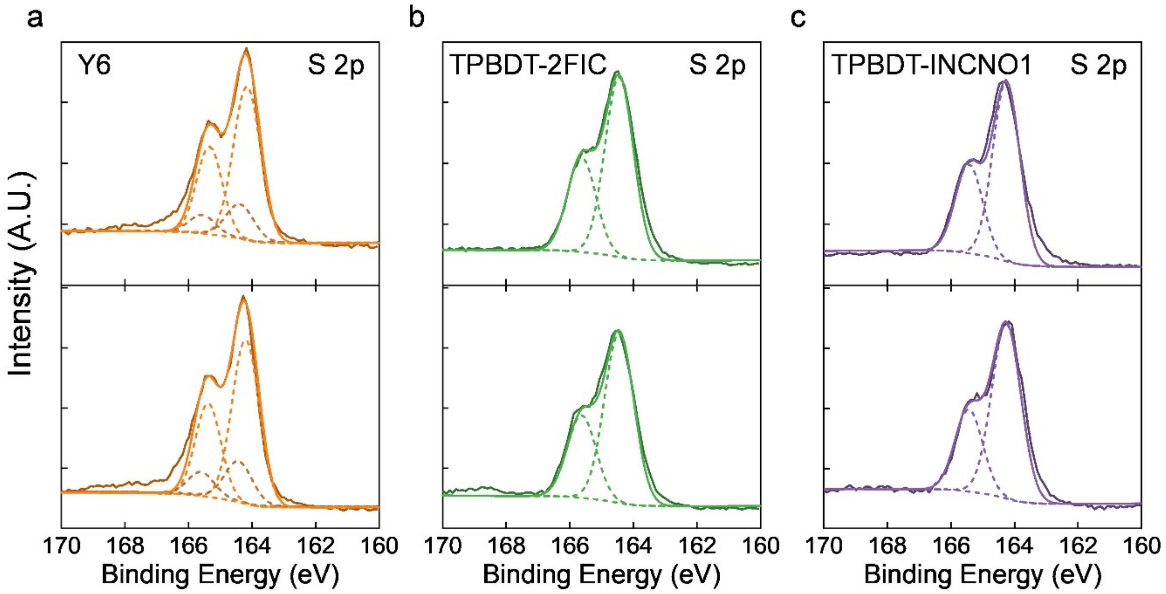

Fig. S24 XPS S 2p spectra of (a) Y6, (b) TPBDT-2FIC, and (c) TPBDT-INCNO1 films before (top) and after (bottom) Pt deposition under 0.2 M AA and 1 sun illumination.

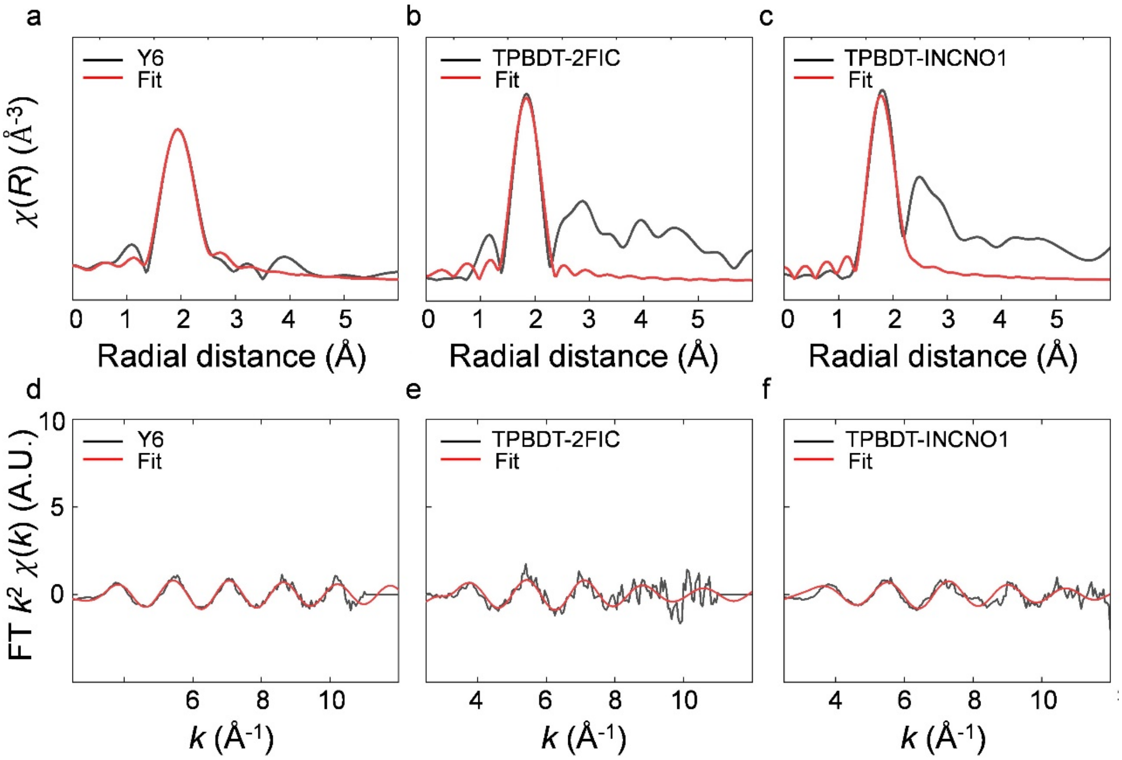

Fig. S25 FT k^2-weight EXAFS fitting curves of Y6, TPBDT-2FIC and TPBDT-INCNO1 NPs at (a-c) *R*- and (d-f) *k*-space. $PtCl_4$ and $PtCl_2(pyridine)_2$ were used as reference compounds for fitting Y6 and TPBDT-based small molecules, respectively.

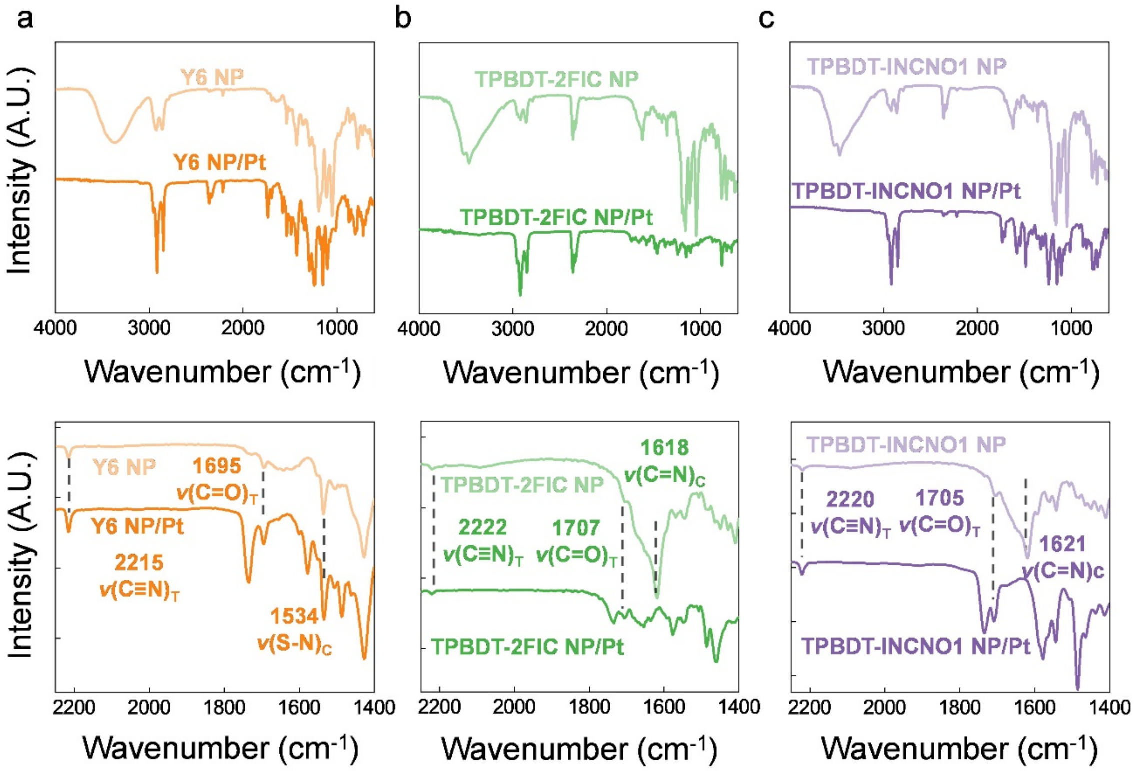

Fig. S26 FT-IR spectra of (a) Y6, (b) TPBDT-2FIC, and (c) TPBDT-INCNO1 NPs before and after Pt deposition, shown across the full spectral range (top, 600–4000 cm^{-1}) and in the magnified region (bottom, 2200–1400 cm^{-1}).

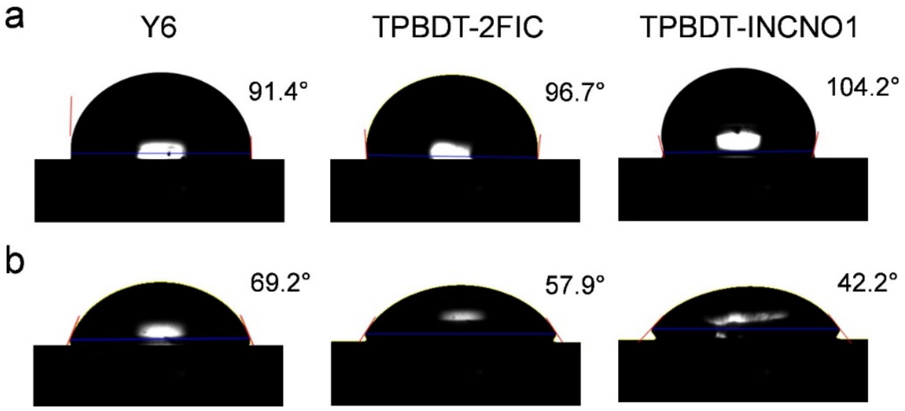

Fig. S27 Water contact angle (a) before and (b) after Pt deposition on small molecule films.

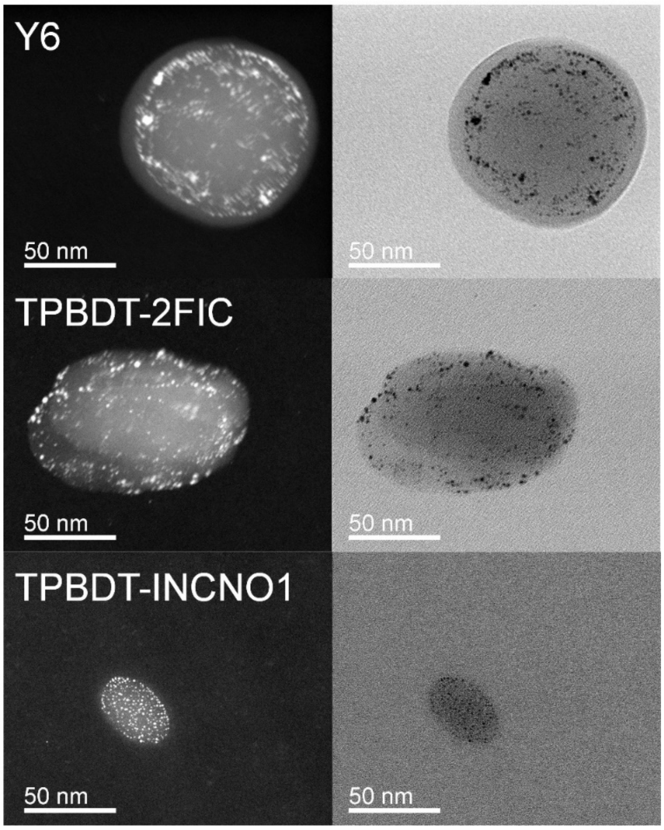

Fig. S28 Dark-field (left) and bright-field (right) STEM images of NPs after 4 h of H_2 generation. The white dots in the dark-field images and the dark dots in the bright-field images indicate the presence of Pt particles.

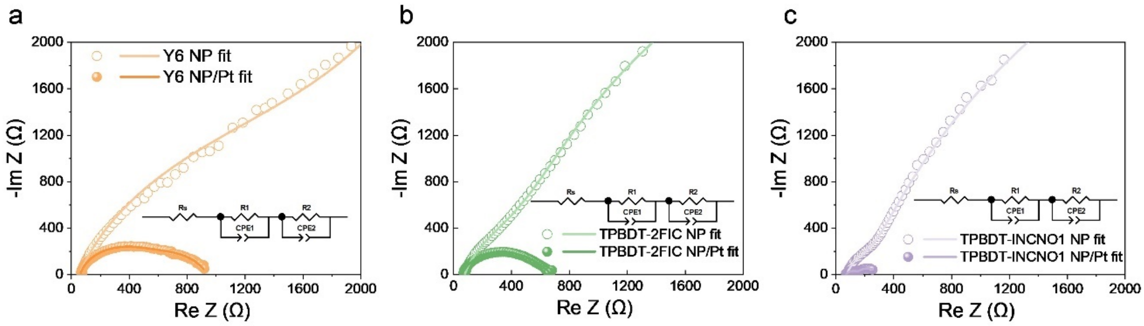

Fig. S29 PEIS Nyquist plots of FTO/NPs and FTO/NPs/Pt electrodes measured in a pH 7 electrolyte under 1 sun illumination for (a) Y6 NPs, (b) TPBDT-2FIC NPs, and (c) TPBDT-INCNO1 NPs before and after Pt deposition.

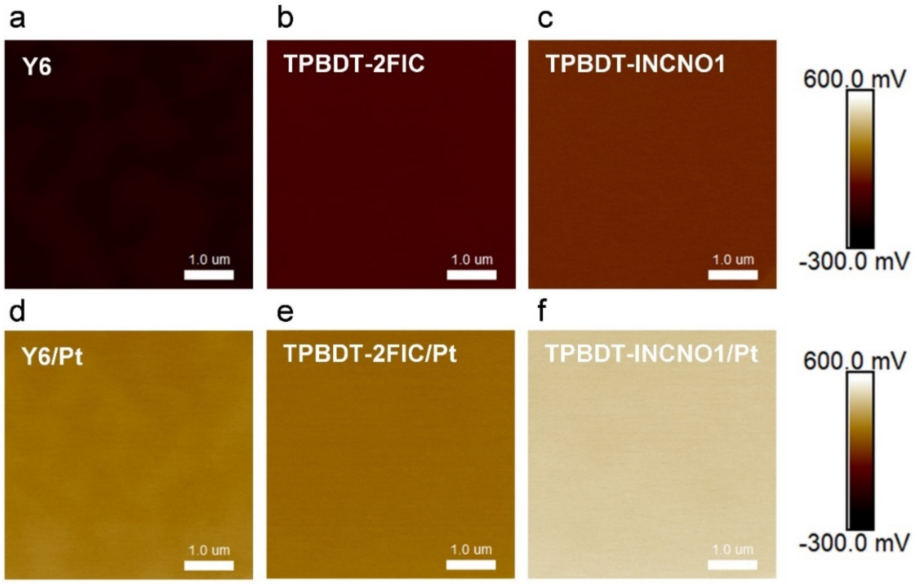

Fig. S30 KPFM images before and after Pt deposition for (a, d) Y6, (b, e) TPBDT-2FIC, and (c, f) TPBDT-INCNO1 films.

KPFM measurements were also conducted to examine the surface work function (WF) after Pt deposition, as shown in Fig. S30. The WF of Y6, TPBDT-2FIC, and TPBDT-INCNO1 films were calculated using the following equation (S6):

$$\varphi_{sample} = \varphi_{tip} - V_{CPD} \quad (S6)$$

where the WF of the tip (φ_{tip}) is 4.72 eV, and V_{CPD} is the contact potential difference. Before Pt deposition, the WFs of Y6, TPBDT-2FIC, and TPBDT-INCNO1 films were determined to be 4.89 eV, 4.71 eV, and 4.59 eV, respectively. After Pt deposition, the WFs shifted to 4.45 eV, 4.46 eV, and 4.26 eV, respectively. The clear WF changes suggest the successful Pt deposition for all cases. It is noteworthy that the WF of TPBDT-INCNO1 after Pt deposition (4.26 eV) becomes closer to the standard hydrogen evolution potential (4.32 eV).[3] This shift in WF is beneficial because it reduces the electron injection barrier at the catalyst-proton interface, facilitating more efficient electron transfer from the catalyst surface to protons. Consequently, this lower energy barrier enhances the catalytic kinetics for hydrogen evolution.

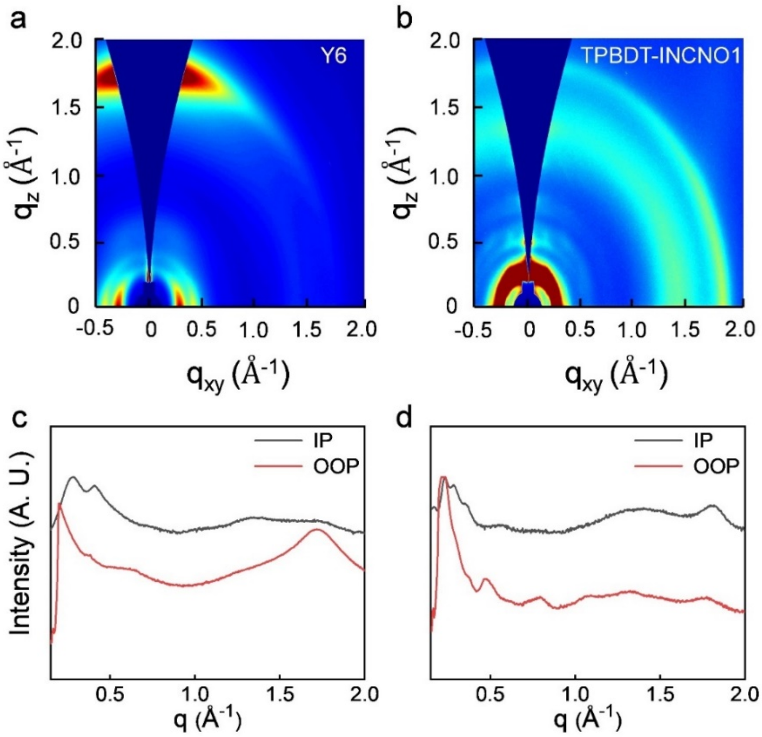

Fig. S31 2D GIWAXS images and corresponding line-cut profiles of (a, c) Y6 and (b, d) TPBDT-INCNO1 thin films.

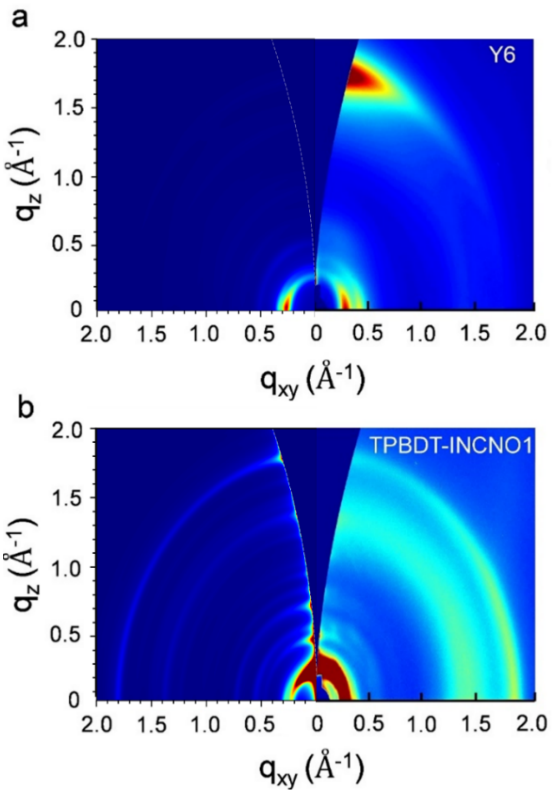

Fig. S32 GIWAXS simulations were performed for thin films of (a) Y6 and (b) TPBDT-INCNO1 films (left: simulated 2D GIWAXS image and right: experimental 2D GIWAXS image).

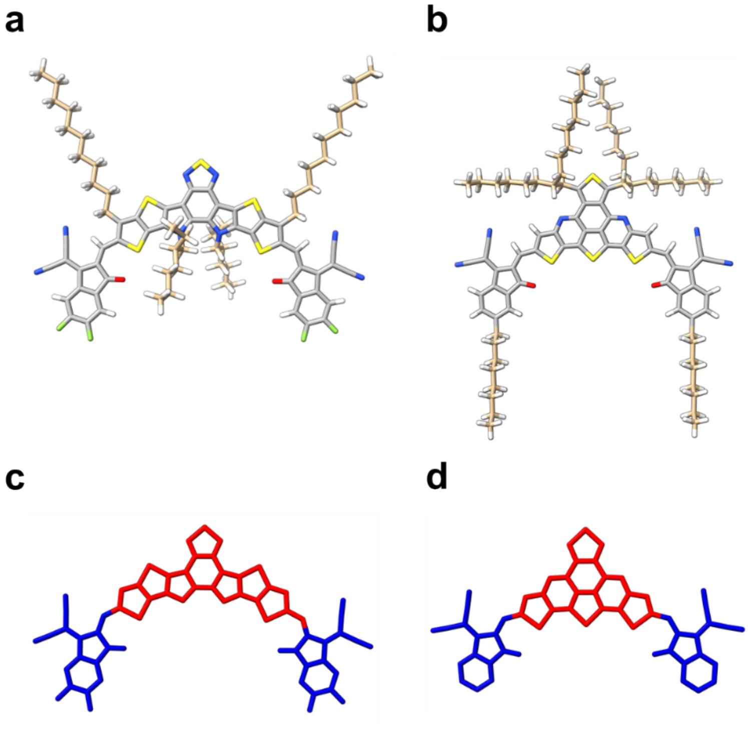

Fig. S33 Optimized geometries of (a) Y6 and (b) TPBDT-INCNO1 were obtained at the B3LYP/6-31+G(d,p) level of theory. Molecular structures were rendered using ChimeraX. The proposed partitioning scheme illustrated in panels (c) and (d) was used to separate the core (red) and end (blue) groups.

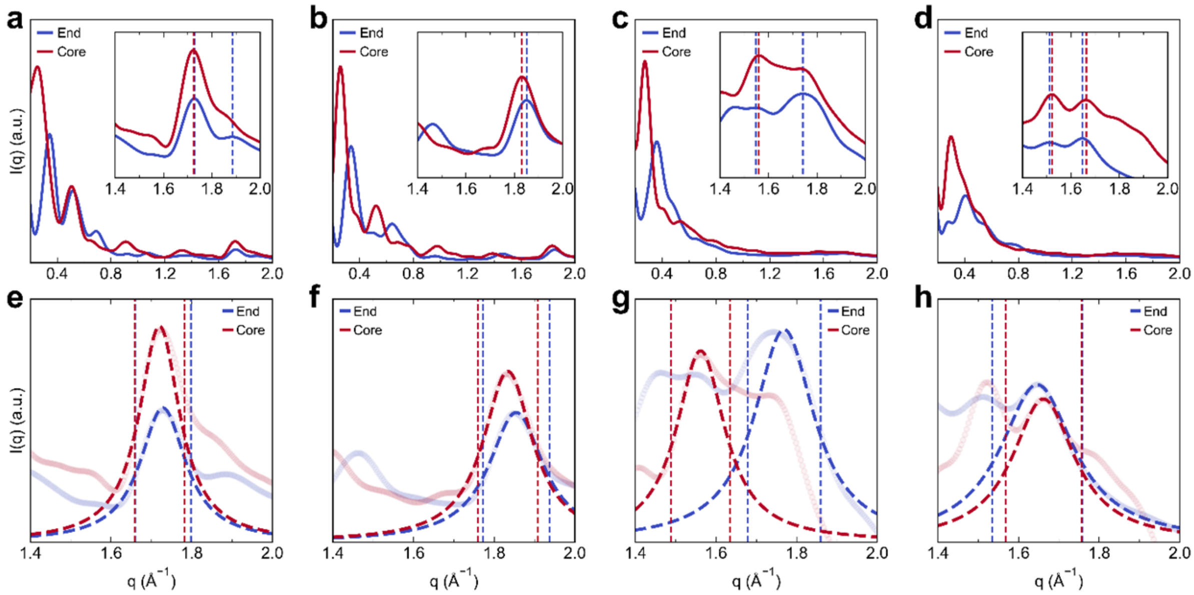

Fig. S34 Debye scattering computations were performed separately on the core and end groups to (a) Y6 and (b) TPBDT-INCNO1 thin films, (c) Y6 and (d) TPBDT-INCNO1 NPs. Insets highlight core-to-core and end-to-end packing regions, with corresponding signals labeled by vertical dashed lines. Panels (e-h) show the best-fit Lorentzian functions used to extract representative packing spacings and the full-width-half-maximum (FWHM) (marked with vertical dashed lines).

Computational details.

The geometries of Y6 and TPBDT-INCNO1 were optimized at the level of theory of B3LYP/6-31+G(d,p) using density functional theory (DFT) in *Jaguar*.[4,5] Optimization was carried out until the energy change and maximum force criteria were below 5×10^{-5} Hartree and 4.5×10^{-4} Hartree/Bohr, respectively. Partial charges were assigned with Mulliken population analysis.[6] The optimized geometries were rendered in Fig. S33a and b. All renderings in this study were produced with ChimeraX.[7]

To simulate the thin film state for Y6 and TPBDT-INCNO1, a unit cell structure proposed in the literature was adapted and modified to include molecules with fully substituted side chains in the initial configurations.[8] Molecular dynamics (MD) simulations were performed to reproduce the packing structure observed in the experimental GIWAXS, using a newly optimized force field developed by our in-house tool, *pyForceTune* (V0.1.9). All simulations were carried out in LAMMPS[9] with GPU acceleration.[10] The following protocol was followed: (1) Upon energy minimization, each simulation was started with periodic boundary conditions (PBCs) using one femtosecond (τ) time step, 13.0 Å van der Waals and 15.0 Å Coulombic interactions cutoffs, and a particle-particle-particle-mesh method[11] with a tolerance of 10^{-5}, (2) The side chains were allowed to relax while constraining the backbone atoms to remain rigid. Systems gradually heated from 0.15 K to 298.15 K in two nanoseconds (ns) under a constant volume using the Nose-Hoover thermostat[12] with a damping factor of 10^2 τ, followed by a 10-ns equilibration in the isothermal-isochoric (NVT) ensemble for final data production. Trajectories were recorded at every 10^5 τ. The cell parameters for Y6 were OA = 25.00 Å, OB = 14.80 Å, OC = 23.00 Å, α=90.0°, β=76.0°, and γ=90.0°. For TPBDT-INCNO1, they were OA = 27.00 Å, OB = 13.92 Å, OC = 22.00 Å, α=90.0°, β=78.0°, γ=90.0°. The OA, OB, and

OC vectors correspond to the experimental crystallographic a, b, and c directions. The OB vector was oriented normal to the AOC plane and aligned to the molecule backbone packing direction. The angles α, β, and γ denote the interaxial angles between vectors OB and OC, OA and OC, and OA and OB, respectively.

To further validate the proposed packing arrangement, the GIWAXS simulations were performed with GIWAXS-Tools[13] for the Y6 and TPBDT-INCNO1 thin film simulations. Simulated scattering vectors were aligned along the OB and OA vectors, corresponding to the face-on orientation in Y6 and edge-on orientation in TPBDT-INCNO1, respectively. To test the energetic favorability of the packing configuration in TPBDT-INCNO1 with fully substituted side chains, a convergence test was conducted using Vienna Ab-initio Simulation Package (VASP)[14, 15] under PBCs. The Perdew, Burke, and Ernzerhof (PBE) exchange-correlation functional[16] with D3 dispersion correction[17] was used to account for van der Waals (vdW) interactions. The projector augmented-wave method[15] was employed with the self-consistency field convergence set to 2×10^{-5} eV. The structural relaxation was carried out until all Cartesian force components were below 0.02 eV Å^{-1}. The cell parameters were successfully optimized using a plane-wave energy cutoff of 520 eV and a $1 \times 2 \times 1$ Γ-centered k-point mesh. Initial configurations for NP simulations of Y6 and TPBDT-INCNO1 were scaled up from their corresponding MD thin film configurations by 2 ×, 4 ×, and 2 × along the OA, OB, and OC directions, respectively, yielding systems containing 64 molecules for each NP simulation. To achieve fully relaxed configurations in the NP systems, we used the Dreiding FF.[18] The applicability of this FF to conjugated systems was demonstrated by our prior study.[19] NP simulations underwent the same MD protocol as the thin film models but without any rigid-body constraints. The final equilibrated frame for each system was placed into a large vacuum box with each dimension set to 150 Å. After 10 ns NVT equilibration for each system, the final configurations are shown in Fig. 3b and d.

Using the last 1-ns trajectories (100 frames) from each system, we performed Debye scattering computations to quantify the packing spacings.[20] Atomic form factors were assigned accordingly. To distinguish spacing from molecular core and end groups separately, we introduced a partitioning scheme (Fig. S33c and d) to isolate the core-to-core (CTC) and end-to-end (ETE) contributions. The Debye scattering profiles are presented in Fig. S34a-d, with CTC and ETE packing regions highlighted. To reduce the contribution from the disordered populations, the baselines for the NPs were corrected consistently. Lorentzian functions were fitted to the identified scattering signals to extract dominant spacing values. We excluded signals with FWHM greater than 0.30 $Å^{-1}$ due to low structural coherence. The best-fit CTC and ETE spacings with minimal FWHM difference were selected as representative packing spacing values.

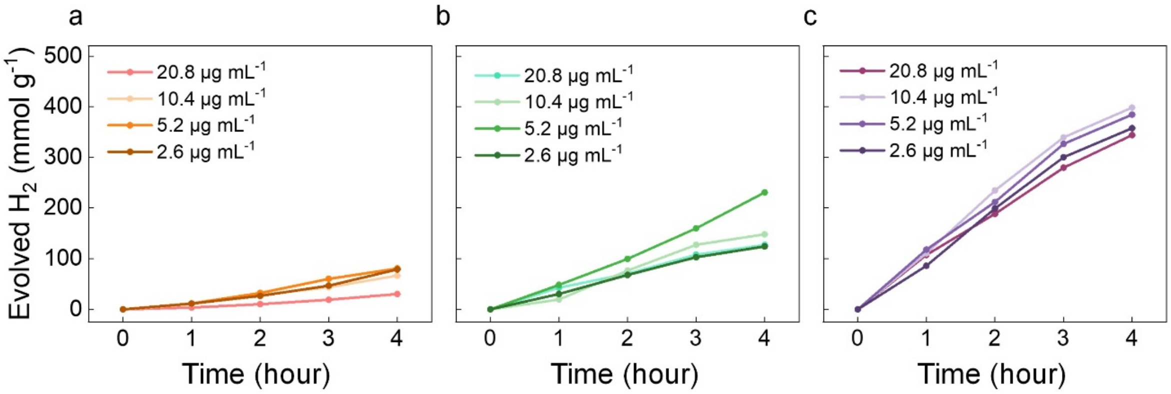

Fig. S35 H_2 generation plots at varying NP concentrations for (a) Y6, (b) TPBDT-2FIC, and (c) TPBDT-INCNO1 NPs under 1 sun illumination in 0.2 M AA solution with 10.1 wt% Pt.

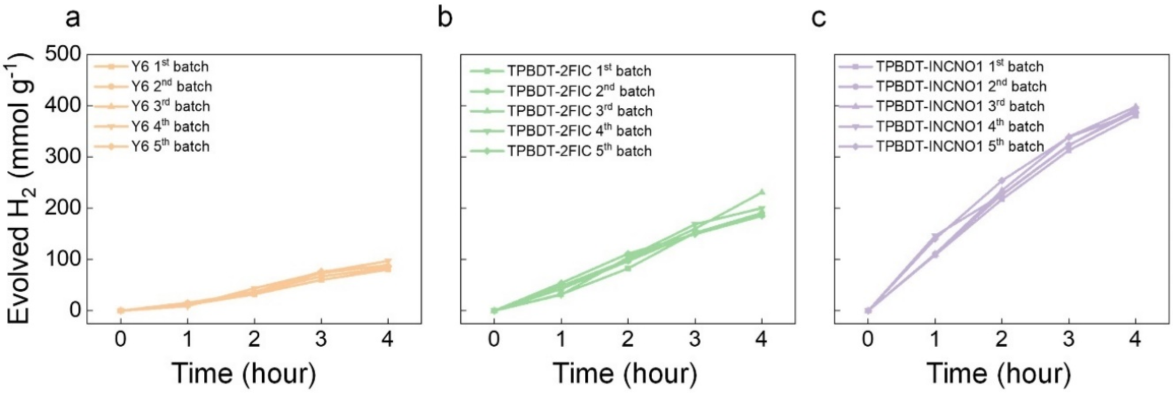

Fig. S36 Reproducibility test of hydrogen evolution using five different NP batches: (a) Y6 (23.2 ± 1.7 mmol h^{-1} g^{-1} at a NP concentration of 5.2 µg mL^{-1}), (b) TPBDT-2FIC (51.2 ± 3.8 mmol h^{-1} g^{-1} at a NP concentration of 5.2 µg mL^{-1}) and (c) TPBDT-INCNO1 (98.3 ± 2.3 mmol h^{-1} g^{-1} at a NP concentration of 10.4 µg mL^{-1}).

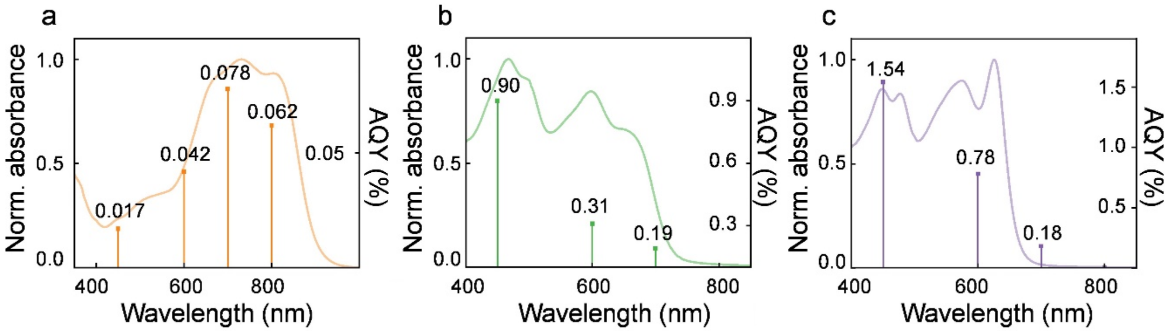

Fig. S37 AQY measurements of (a) Y6, (b) TPBDT-2FIC, and (c) TPBDT-INCNO1 NPs (10.4 μg mL^{-1}, 0.2 M AA and 10.1 wt% Pt) under monochromatic light illumination at 450, 600, 700, and 800 nm.

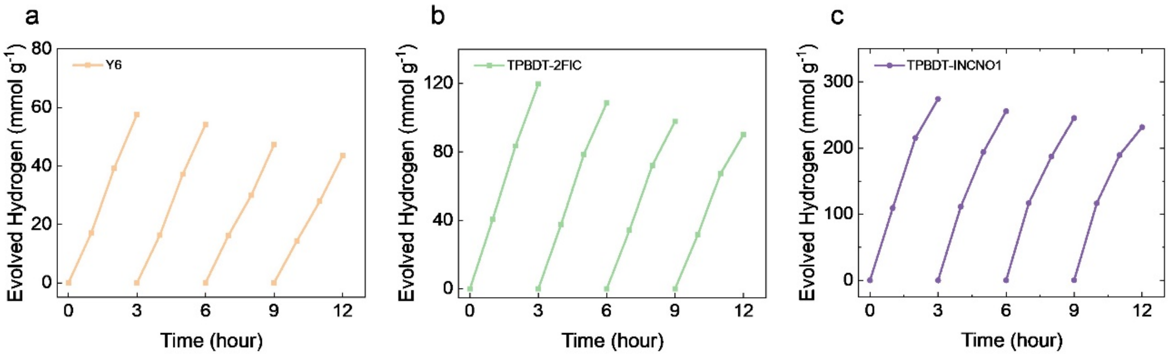

Fig. S38 Photocatalytic cycling stability test of (a) Y6, (b) TPBDT-2FIC, and (c) TPBDT-INCNO1 NPs (10.4 μg mL^{-1}, 0.2 M AA and 10.1 wt% Pt).

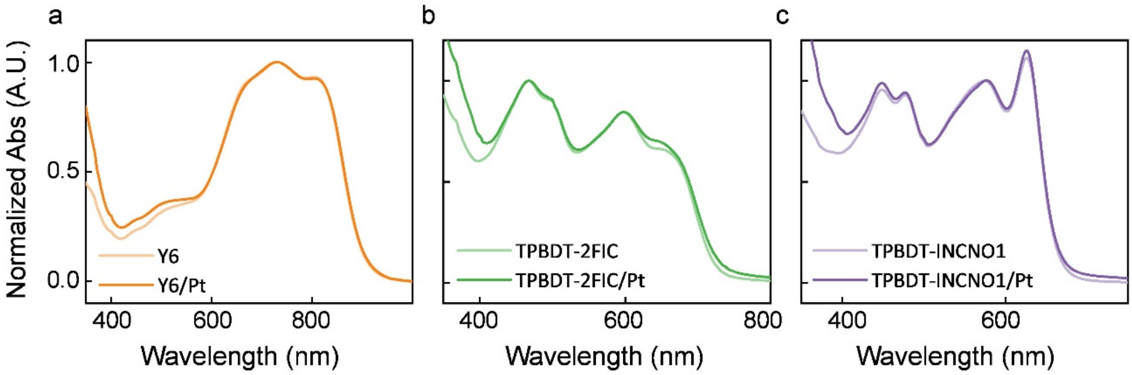

Fig. S39 UV-Vis spectra of (a) Y6, (b) TPBDT-2FIC, and (c) TPBDT-INCNO1 NPs before and after 12 h photocatalytic H_2 production.

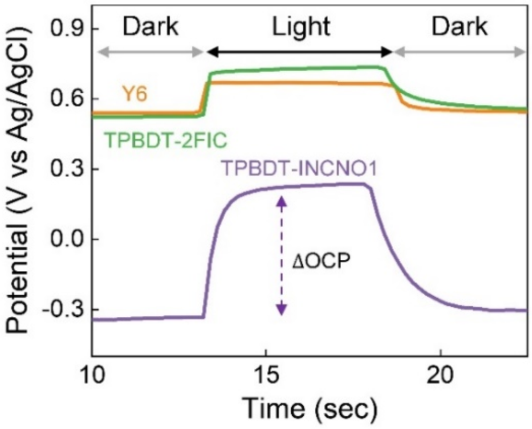

Fig. S40 OCP curves of FTO/[2-(9H-carbazol-9-yl)ethyl]phosphonic acid (2PACz)/photoactive layer film/Pt device under chopped light illumination.

Furthermore, open-circuit potential (OCP) measurements on the films provide insights into the intrinsic photovoltage generation capability under illumination, reflecting the effective charge separation and driving force available at the photocatalyst/electrolyte interface.[21,22] The *Δ*OCP plots (the difference between the OCP measured in the dark and under illumination) for each molecule were determined to be 0.13 V, 0.21 V, and 0.58 V for Y6, TPBDT-2FIC, and TPBDT-INCNO1 films, respectively (Fig. S40). The significantly higher *Δ*OCP of TPBDT-INCNO1 suggests a higher photovoltage generation under light, which can be attributed to its larger bandgap, providing a stronger thermodynamic driving force for H_2 generation reaction.

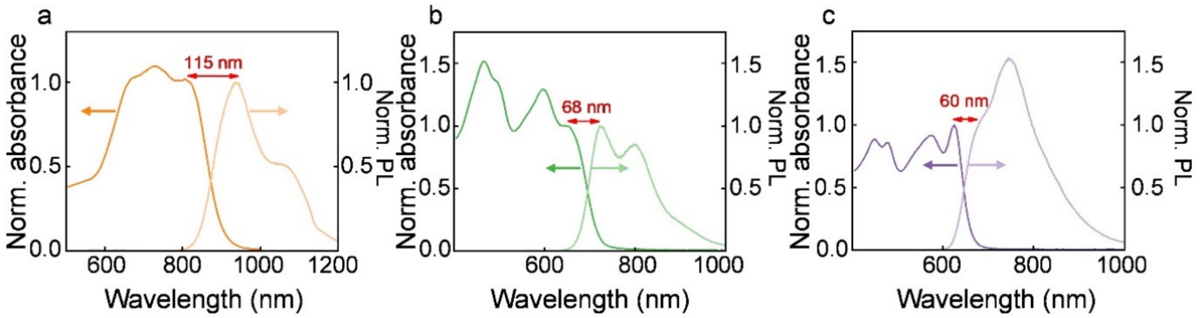

Fig. S41 Stokes shifts of (a) Y6, (b) TPBDT-2FIC and (c) TPBDT-INCNO1 NP suspensions.

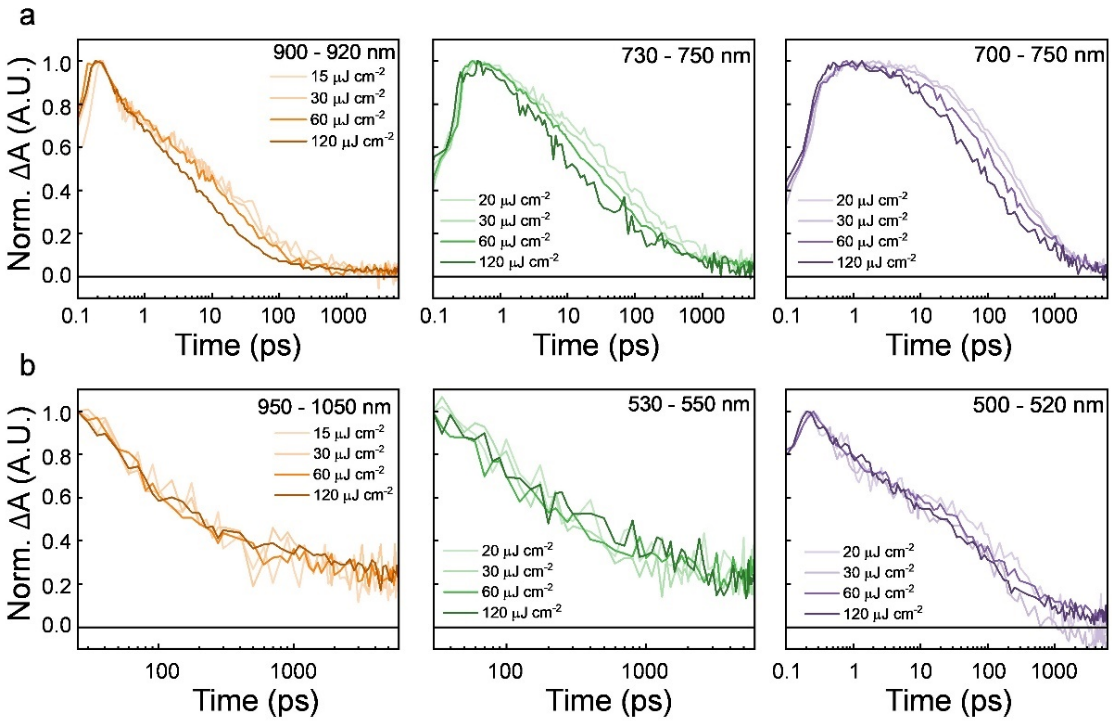

Fig. S42 Normalized (a) exciton and (b) charge kinetics in Y6 (left), TPBDT-2FIC (middle), and TPBDT-INCNO1 NPs (right).

Detailed TAS spectra analysis.

Y6 NPs displayed a ground-state bleaching (GSB) peak at 660 nm and a photoinduced absorption (PIA) peak at 910 nm. The 910 nm PIA exhibited fluence-dependent kinetics characteristic of exciton–exciton annihilation (EEA), as well as an ultrafast (<ps), fluence-independent decay, assigned to the formation of pseudo charge transfer (CT) or intermolecular excitonic states within ~0.2 ps, as reported for Y6 films.[23] At later times, a long-lived positive feature spanning 900–1100 nm was observed with fluence-independent decay, likely corresponding to charge species. TPBDT-2FIC NPs showed GSB peaks at 475, 510, and 680 nm, along with PIA peaks at 530 and 750 nm. The fluence-dependent decay at 750 nm further confirmed the presence of singlet excitons (Fig. S42a), while the fluence-independent decay at 530 nm (Fig. S42b) indicated the presence of CT species. TPBDT-INCNO1 NPs exhibited distinct GSB peaks at 480, 550, and 630 nm, with PIA bands centered at 510 nm and spanning the 700–750 nm range. The 700–750 nm PIA region showed fluence-dependent decay behavior, whereas the 510 nm PIA feature displayed fluence-independent kinetics, more indicative of CT species (Fig. S42). We noted that the small discrepancy between TRPL and TAS data for TPBDT-2FIC and Y6 exciton lifetimes is likely due to residual EEA effects at the higher excitation densities (>3 μJ cm^{-2}) required for TAS measurements.

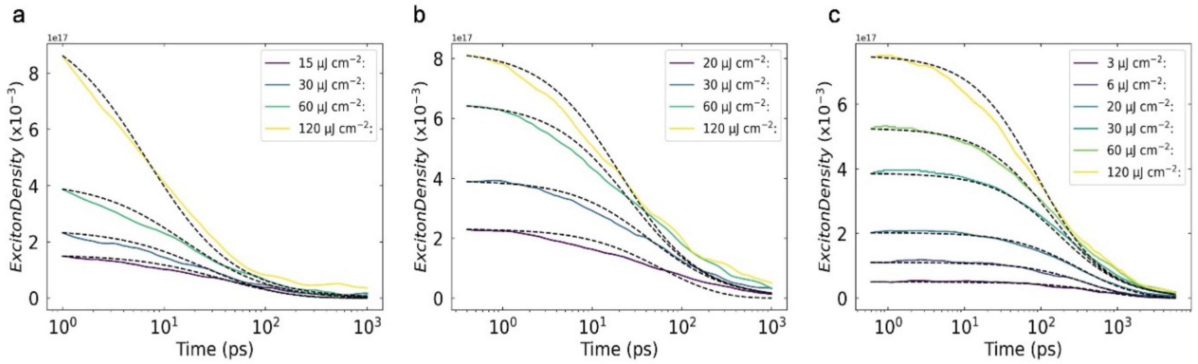

Fig. S43 Fitted exciton kinetics of (a) Y6, (b) TPBDT-2FIC, and (c) TPBDT-INCNO1 NPs by the EEA model.

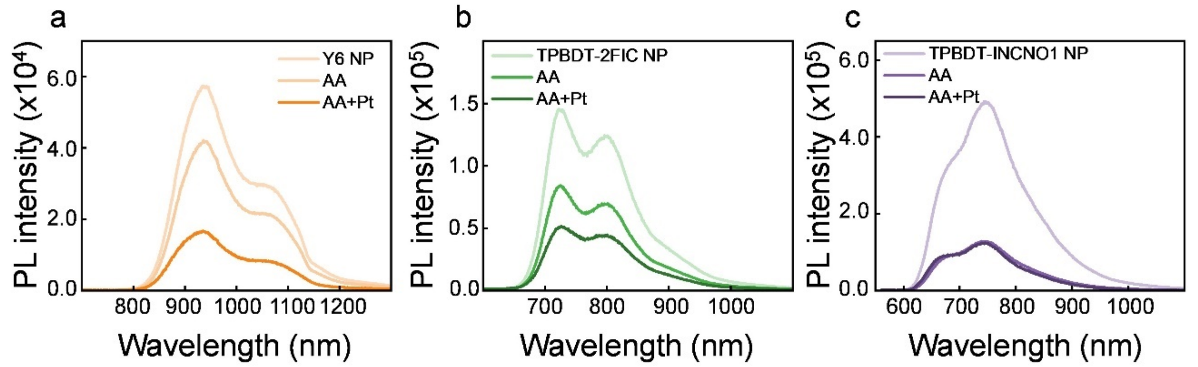

Fig. S44 Steady-state PL spectra of (a) Y6, (b) TPBDT-2FIC and (c) TPBDT-INCNO1 NP suspensions with DI water only, AA (0.2 M), and AA (0.2 M) with Pt (10.1 wt%). (corrected for sample absorption).

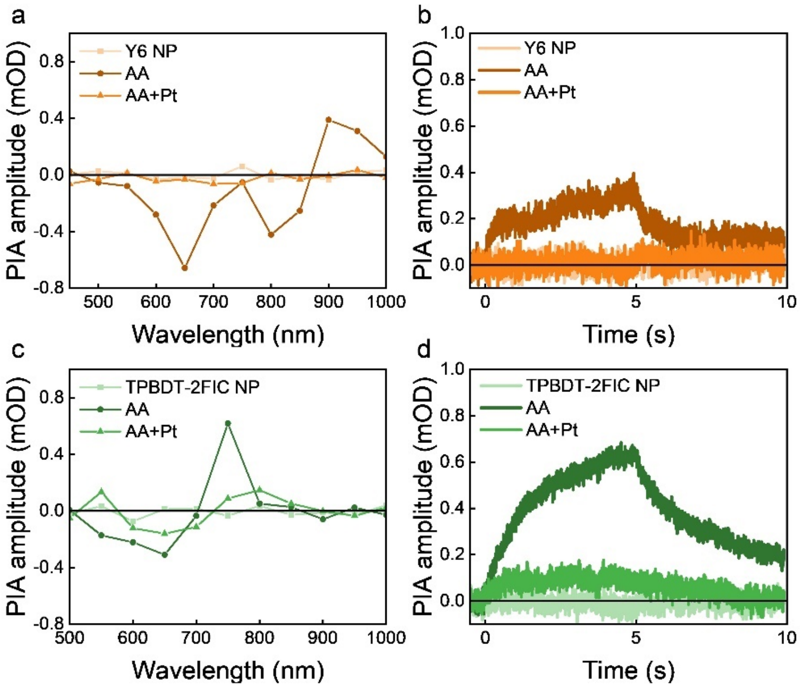

Fig. S45 (a) PIA spectrum and (b) kinetics of Y6 NP suspension at 900 nm with AA (0.2 M) and AA (0.2 M) with Pt (10.1 wt%). (c) PIA spectrum and (d) kinetics of TPBDT-2FIC NP suspension at 750 nm with AA (0.2 M) and AA (0.2 M) with Pt (10.1 wt%).

Table S1 EXAFS fitting parameters for Y6, TPBDT-2FIC, and TPBDT-INCNO1.

Sample	Shell	CN	σ^2 [10^{-3} Å^2]	ΔE_0 [eV]	ΔR [Å]	R [Å]
Y6	Pt-Cl	3.73	0.5	4.66	0.0005	2.33
TPBDT-2FIC	Pt-N	2.27	2.2	1.63	0.08	2.11
	Pt-Cl	3.17	5.3	8.3	0.06	2.25
TPBDT-INCNO1	Pt-N	2.05	1.3	3.03	0.04	2.07
	Pt-Cl	2.69	4.4	9.54	0.06	2.25

*CN, coordination number; σ^2, Debye-Waller factors (a measure of thermal and static disorder in absorber-scatterer distances); ΔE_0: inner potential correction (the difference between the zero kinetic energy value of the sample and that of the theoretical model); *R*, distance between absorber and backscatter atoms. **The amplitude reduction factor (S_0^2) was fixed at 0.85. Typical error estimates for the fitting parameters are $0.001 < \sigma^2 < 0.01$, $\Delta E_0 \pm 10$ eV, and $\Delta R \pm 0.1$ Å.

Table S2. Fitted PEIS parameters for FTO/NPs and FTO/NPs/Pt electrodes.

	R_s (Ω)	R_1 (kΩ)	R_2 (kΩ)
Y6	52	1.71	80.2
Y6/Pt	60	0.43	0.44
TPBDT-2FIC	75	0.15	10.5
TPBDT-2FIC/Pt	60	0.18	0.43
TPBDT-INCNO1	77	0.45	8.6
TPBDT-INCNO1/Pt	72	0.08	0.13

R_1 is assigned to the charge-transport resistance (R_{trans}), and R_2 corresponds to the interfacial charge-transfer resistance (R_{ct}).

Table S3 GIWAXS packing parameters of Y6 and TPBDT-INCNO1 thin films.

Compound	Direction	*q* [Å^{-1}]	*d*-spacing [Å]	FWHM [Å^{-1}]	CCL [Å]
Y6	In-plane	0.2765	22.72	0.0877	64.5
		0.4102	15.32	0.1110	51.0
	Out-of-plane	1.7164	3.66	0.2005	28.5
TPBDT-INCNO1	In-plane	0.2330	26.97	0.0376	150.5
		1.8077	3.48	0.1327	43.2
	Out-of-plane	0.4755	26.42	0.1015	55.8
		0.7865	23.97	0.1568	36.2
		1.0723	23.44	0.1681	33.8
		1.7500	3.59	0.2569	22.3

Table S4 Simulated core-to-core (CTC) and end-to-end (ETE) spacing data obtained from Debye scattering and Lorentzian fitting.

	Packing	*q* [Å^{-1}]	*d*-spacing [Å]	FWHM [Å^{-1}]
Y6 (Film)	CTC	1.7240	3.64	0.1227
	ETE	1.7287	3.63	0.1384
TPBDT-INCNO1 (Film)	CTC	1.8312	3.43	0.1488
	ETE	1.8513	3.39	0.1646
Y6 (NP)	CTC	1.5597	4.03	0.1464
	ETE	1.7422	3.61	0.1803
TPBDT-INCNO1 (NP)	CTC	1.6633	3.78	0.1882
	ETE	1.6489	3.81	0.2233

Table S5 HER efficiency with different NP concentrations (under 10.1 wt% of Pt, 0.2 M AA, 1 sun illumination).

NP concentration [μg mL^{-1}]	Y6 [mmol h^{-1} g^{-1}]	TPBDT-2FIC [mmol h^{-1} g^{-1}]	TPBDT-INCNO1 [mmol h^{-1} g^{-1}]
20.8	7.6	32.0	86.0
10.4	16.6	40.5	102.5
5.2	21.0	57.3	97.7
2.6	19.2	32.1	80.94

Table S6 Summary of PL decay lifetimes and PLQY values and calculated radiative (k_r) and nonradiative (k_{nr}) decay rate values for neat NP suspensions.

Sample	τ_{PL} [ns]	PLQY [%]	k_r [ns^{-1}]	k_{nr} [ns^{-1}]
Y6	0.41	0.2	0.005	2.43
TPBDT-2FIC	0.72	4.0	0.05	1.34
TPBDT-INCNO1	1.66	10	0.06	0.54

Radiative and non-radiative decay calculation.

For a sample with an exponential PL decay, the PLQY (Φ) is expressed as

$$\Phi = \frac{number\ of\ photons\ emitted}{number\ of\ photons\ absorbed} = \frac{k_r}{k_r + k_{nr}} \quad (S7)$$

where k_r is the radiative decay rate, and k_{nr} is the sum of all non-radiative decay rates.

At low excitation densities where charge recombination is negligible, charge generation can be considered a non-radiative decay pathway. The exponential lifetime of the PL decay, τ_{PL}, is related to the decay rates by the equation S8

$$\tau_{PL} = \frac{1}{k_r + k_{nr}} \quad (S8)$$

The calculated k_r and k_{nr} are summarized in Table S6.

Table S7 Parameters of exciton diffusion length (L_D) global fittings for NP suspensions.

Sample	R [nm]	τ [ns]$^{b)}$	α [10^{-7} cm^3 s^{-1}]	D [10^{-2} cm^2 s^{-1}]	L_D [nm]	$L_{D.\ Avg.}$ [nm]
Y6	2.3$^{a)}$	0.41	2.12	3.67	38.8	48 ± 10
	1.0			8.44	58.8	
TPBDT-2FIC	1.8$^{a)}$	0.72	0.73	2.90	31.5	38 ± 7
	1.0			1.61	45.7	
TPBDT-INCNO1	2.4$^{a)}$	1.66	0.38	0.63	32.3	41 ± 9
	1.0			1.51	49.9	

R, annihilation radius; τ, exciton lifetime; α, bimolecular singlet–singlet exciton annihilation rate constant; D, exciton diffusion coefficient. $^{a)}$ R is d_{100} spacings extracted from GIWAXS data. $^{b)}$ Exciton lifetimes measured by TRPL.

Exciton diffusion length.

For TPBDT-INCNO1, L_D is estimated as ~ 50 nm (upper limit) assuming a typical annihilation radius of 1 nm,[24,25] or ~32 nm (lower limit) when using a 2.4 nm annihilation radius derived from the d_{100} spacing measured by GIWAXS of neat films. TPBDT-2FIC exhibited shorter L_D values of ~31 nm (upper limit) and ~46 nm (lower limit), consistent with its shorter exciton lifetime. However, for Y6, the estimated L_D values do not align with the observed exciton lifetime trend. The lower estimate (~39 nm) matches previously reported diffusion lengths for Y6 films (~37 nm),[24] but the upper estimate (~59 nm) exceeds those of both TPBDT-INCNO1 and TPBDT-2FIC.

This discrepancy may arise from the estimation of the annihilation rate constant (α) from TAS decay kinetics. As discussed, exciton–exciton annihilation (EEA) is likely present even at the lowest excitation fluences for TPBDT-2FIC and Y6, leading to an overestimation of α because nonlinear decay components attributed to EEA are significant even at low excitation densities. Furthermore, the assignment of singlet excitons in the TAS spectra of Y6 is controversial. Here, the exciton signals tracked in Y6 are likely influenced by pseudo-CT or intermolecular exciton states that form within ~0.2 ps. Consequently, the calculated L_D values for TPBDT-2FIC and Y6 are probably overestimated.

Although the exciton diffusion lengths for TPBDT-2FIC (~31-46 nm) and Y6 (~39-59 nm) are likely overestimated, they remain substantially shorter than their respective average NP sizes (~125 nm for TPBDT-2FIC and ~82 nm for Y6). This mismatch between diffusion length and particle size likely limits exciton diffusion to the NP interface before recombination. Given that TPBDT-INCNO1 has the smallest average NP radius (~35 nm), its long exciton diffusion length of approximately 32–50 nm enables efficient exciton diffusion to the NP interface.

Table S8 TRPL lifetime changes of NPs in pure water, in the presence of AA (0.2 M) and in the presence of AA (0.2 M) with Pt (10.1 wt%).

NP	TRPL Lifetime [ns]		
	H_2O	0.2 M AA	0.2 M AA with Pt
Y6	0.41	0.35	0.24
TPBDT-2FIC	0.72	0.61	0.57
TPBDT-INCNO1	1.66	0.77	0.74

Table S9 Estimated hole transfer rate (k_{ht}) and time (τ_{ht}) from TRPL lifetime measurements.

NP	k_{ht} [ns^{-1}]	τ_{ht} [ns]
Y6	0.42	2.4
TPBDT-2FIC	0.25	4.0
TPBDT-INCNO1	0.70	1.4

Hole Transfer Rate Calculation.

To calculate the hole transfer rate (k_{ht}) from TRPL lifetime data with and without AA, we derive the equation based on TRPL lifetime quenching, assuming that the quenching is solely due to hole transfer (no energy transfer or other decay pathways).[26] This is validated by ensuring no spectral overlap between the emission of the PC and absorption of AA. In addition, AA is present in excess, so the rate is independent of its concentration.

Here's the derivation:

The exciton lifetime (τ_{NP}) is governed by intrinsic recombination (S9):

$$\frac{1}{\tau_{NP}} = k_{recomb} \qquad \text{(S9)}$$

where k_{recomb} is the intrinsic recombination rate.

Adding AA introduces a hole transfer pathway (k_{ht}) (S10),

$$\frac{1}{\tau_{NP\,+\,AA(0.2M)}} = k_{recomb} + k_{ht} \qquad \text{(S10)}$$

so, hole transfer rate (k_{ht}) equals to (S11)

$$k_{ht} = \frac{1}{\tau_{NP\,+\,AA(0.2M)}} - \frac{1}{\tau_{NP}} \quad (S11)$$

where hole transfer time (τ_{ht}) is (S12)

$$\tau_{ht} = \frac{1}{k_{ht}} \quad (S12)$$

References.

1. X. Li, G. Huang, H. Jiang, S. Qiao, X. Kang, W. Chen and R. Yang, *J. Mater. Chem. C* 2019, **7**, 6105-6111.

2. W. Sun, S. Gámez-Valenzuela, X. Zhang, J.-W. Lee, Z. Zhong, P. Wang, S. Ma, H. Wang, B. J. Kim and X. Guo, *Angew. Chem. Int. Ed.* 2025, **64**, e202501196.

3. J. Kosco, M. Bidwell, H. Cha, T. Martin, C. T. Howells, M. Sachs, D. H. Anjum, S. Gonzalez Lopez, L. Zou, A. Wadsworth, W. Zhang, L. Zhang, J. Tellam, R. Sougrat, F. Laquai, D. M. DeLongchamp, J. R. Durrant and I. McCulloch, *Nat. Mater.* 2020, **19**, 559-565.

4. A. D. Becke, *Phys. Rev. A* 1988, **38**, 3098.; C. Lee, W. Yang and R. G. Parr, *Phys. Rev. B* 1988, **37**, 785.

5. A. D. Bochevarov, E. Harder, T. F. Hughes, J. R. Greenwood, D. A. Braden, D. M. Philipp, D. Rinaldo, M. D. Halls, J. Zhang and R. A. Friesner, *Int. J. Quantum Chem.* 2013, **113**, 2110-2142.

6. R.S Mulliken, *J. Chem. Phys.* 1955, **23**, 1833-1840.

7. E. C. Meng, T. D. Goddard, E. F. Pettersen, G. S. Couch, Z. J. Pearson, J. H. Morris and T. E. Ferrin, *Protein Sci.* 2023, **32**, e4792.

8. G. Zhang, X. -K. Chen, J. Xiao, P. C. Chow, M. Ren, G. Kupgan, X. Jiao, C. C. Chan, X. Du and R. Xia, *Nat. Commun.* 2020, **11**, 3943.

9. A. P. Thompson, H. M. Aktulga, R. Berger, D. S. Bolintineanu, W. M. Brown, P. S. Crozier, P. J. In't Veld, A. Kohlmeyer, S. G. Moore, T. D. Nguyen, R. Shan, M. J. Stevens, J. Tranchida, C. Trott and S. J. Plimpton, *Comput. Phys. Commun.* 2022, **271**, 108171.

10. T. D. Nguyen, *Comput. Phys. Comm.* 2017, **212**, 113-122.

11. M. Deserno and C. Holm, *J. Chem. Phys.* 1998, **109**, 7678-7693.

12. W. G. Hoover, *Phys. Rev. A* 1985, **31**, 1695.

13. Y. Pan, J. Huang, D. Gao, Z. Chen, W. Zhang and G. Yu, *Polym. Chem.* 2021, **12**, 2471-2480.; D. W. Breiby, O. Bunk, J. W. Andreasen, H. T. Lemke and M. M. Nielsen, *J. Appl. Crystallogr.* 2008, **41**, 262-271.

14. G. Kresse and J. Hafner, *Phys. Rev. B* 1993, **47**, 558.

15. G. Kresse and D. Joubert, *Phys. Rev. B* 1999, **59**, 1758.

16. J. P. Perdew, K. Burke and M. Ernzerhof, *Phys. Rev. Lett.* 1996, **77**, 3865.

17. S. Grimme, S. Ehrlich and L. Goerigk, *J. Comput. Chem.* 2011, **32**, 1456-1465.

18. S. L. Mayo, B. D. Olafson and W. A. Goddard, *J. Phys. Chem.* 1990, **94**, 8897-8909.; K. I. Kim, R. Lawler, H. J. Moon, P. Narayanan, M. A. Sakwa-Novak, C. W. Jones and S. S. Jang, *ACS Omega* 2021, **6**, 3390-3398.

19. Z. Wang, D. Zhang, L. Yang, O. Allam, Y. Gao, Y. Su, M. Xu, S. Mo, Q. Wu and Z. Wang, *Science* 2025, **387**, 381-387.

20. P. Debye, *Physik. Z.* 1930, **31**, 419-428.; L. Gelisio and P. Scardi, *Acta Crystallogr. A* 2016, **72**, 608-620.; H. Makki, C. A. Burke and A. Troisi, *J. Phys. Chem. Lett.* 2023, **14**, 8867-8873.

21. S. P. Berglund, F. F. Abdi, P. Bogdanoff, A. Chemseddine, D. Friedrich and R. Van de Krol, *Chem. Mater.* 2016, **28**, 4231-4242.

22. J. Su, C. Liu, D. Liu, M. Li and J. Zhou, *ChemCatChem* 2016, **8**, 3279-3286.

23. R. Wang, C. Zhang, Q. Li, Z. Zhang, X. Wang and M. Xiao, *J. Am. Chem. Soc.* 2020, **142**, 12751–12759.

24. Y. Firdaus, V. M. L. Corre, S. Karuthedath, W. Liu, A. Markina, W. Huang, S. Chattopadhyay, M. M. Nahid, M. I. Nugraha, Y. Lin, A. Seitkhan, A. Basu, W. Zhang, I. McCulloch, H. Ade, J. Labram, F. Laquai, D. Andrienko, L. J. A. Koster and T. D. Anthopoulos, *Nat. Commun.* 2020, **11**, 5220.

25. S. Chandrabose, K. Chen, A. J. Barker, J. J. Sutton, S. K. K. Prasad, J. Zhu, J. Zhou, K. C. Gordon, Z. Xie, X. Zhan and J. M. Hodgkiss, *J. Am. Chem. Soc*. 2019, **141**, 6922–6929.

26. D. Venkateswarlu, T. Swetha, S. Akhil, M. Palabathuni, N. Mishra and S. P. Singh, *Mater. Adv*. 2023, **4**, 1935-1940.